980030

The Aerodynamic Performance of Automotive Underbody Diffusers

Kevin R. Cooper, T. Bertenyi, G. Dutil and J. Syms
National Research Council of Canada

G. Sovran
GM Research, Retired

Reprinted From: Developments in Vehicle Aerodynamics (SP-1318)



International Congress and Exposition Detroit, Michigan February 23-26, 1998

Tel: (724) 776-4841 Fax: (724) 776-5760

The appearance of this ISSN code at the bottom of this page indicates SAE's consent that copies of the paper may be made for personal or internal use of specific clients. This consent is given on the condition, however, that the copier pay a \$7.00 per article copy fee through the Copyright Clearance Center, Inc. Operations Center, 222 Rosewood Drive, Danvers, MA 01923 for copying beyond that permitted by Sections 107 or 108 of the U.S. Copyright Law. This consent does not extend to other kinds of copying such as copying for general distribution, for advertising or promotional purposes, for creating new collective works, or for resale.

SAE routinely stocks printed papers for a period of three years following date of publication. Direct your orders to SAE Customer Sales and Satisfaction Department.

Quantity reprint rates can be obtained from the Customer Sales and Satisfaction Department.

To request permission to reprint a technical paper or permission to use copyrighted SAE publications in other works, contact the SAE Publications Group.



All SAE papers, standards, and selected books are abstracted and indexed in the Global Mobility Database

No part of this publication may be reproduced in any form, in an electronic retrieval system or otherwise, without the prior written permission of the publisher.

ISSN 0148-7191

Copyright 1998 Society of Automotive Engineers, Inc.

Positions and opinions advanced in this paper are those of the author(s) and not necessarily those of SAE. The author is solely responsible for the content of the paper. A process is available by which discussions will be printed with the paper if it is published in SAE Transactions. For permission to publish this paper in full or in part, contact the SAE Publications Group.

Persons wishing to submit papers to be considered for presentation or publication through SAE should send the manuscript or a 300 word abstract of a proposed manuscript to: Secretary, Engineering Meetings Board, SAE.

Printed in USA

The Aerodynamic Performance of Automotive Underbody Diffusers

Kevin R. Cooper, T. Bertenyi, G. Dutil and J. Syms
National Research Council of Canada

G. Sovran GM Research, Retired

Copyright © 1998 Society of Automotive Engineers, Inc.

ABSTRACT

This paper examines the aerodynamic behaviour of plane-walled, single-plane-expansion, underbody diffusers fitted to a wind-tunnel model of a wheel-less, simple body having automobile proportions. The measurements were performed over a moving-belt assembly in the Pilot Wind Tunnel of the National Research Council of Canada (NRC). The purposes of the investigation were:

- to understand the governing physics of automotive underbody diffusers operating in ground proximity,
- to examine the effect of moving-ground and fixedground simulations on the behaviour of such diffusers and on the corresponding vehicle downforce and drag,
- to map the performance of simple, quasi-two-dimensional diffusers when used to produce downforce or drag reduction.

The paper concentrates on the physics of the underbody flow in an attempt to understand diffuser behaviour in this application and its effect on downforce and drag, and to gain new insight into the relative characteristics of different vehicle ground simulations.

The data are analysed from the diffuser perspective by relating the measurements to the conventional diffuser parameters of area ratio, non-dimensional length and flow-area blockage. This last parameter, which represents the velocity non-uniformity in the inlet flow due to boundary layers on the underside of the model and on the tunnel floor, is one that may contribute to diffuser performance differences between the fixed-ground and the moving-ground simulations.

A performance characteristic defining diffuser geometries for maximum downforce has been identified. Knowledge of its functional behaviour offers the possibility of developing similar curves for new vehicle geometries with a reduced number of measurements or computations.

The data acquired demonstrate that an underbody diffuser can significantly increase downforce, and can provide some drag reduction if ride height is not too small.

INTRODUCTION

The racing community has used underbody diffusers in ground-effect racing cars for many years to develop large downforce as an aid to braking, cornering and acceleration performance [1]. More recently, the passenger-car industry, in search of reduced drag, efficient cooling and improved handling, has shown increased interest in the improvement of underbody flows. In one case [2], an underbody diffuser was used in the development of a passenger car with a drag coefficient of 0.26.

Although widely used for racing and of growing interest for passenger-car applications, little data can be found on the subject of underbody diffuser performance. More importantly, the flow physics of such diffusers have not been well explored. An important aspect of diffuser behaviour that is not understood in the underbody application is its interaction with the ground. A moving-ground simulation is commonly used for racing applications, where ride heights are very small and underbody flows are important, while most road-vehicle developments are performed over a fixed floor. Recently, the question of whether a moving-ground simulation is necessary for passenger-car underbody development has come to the fore [3,4]. Criteria for determining when a fixed-ground simulation is adequate and when a moving-ground simulation is necessary do not yet exist.

George & Donis [5] examined diffuser behaviour and presented useful insight into the underbody flow physics by identifying a vortex pair that was induced on the sides of the diffuser surface by lateral inflows into the underbody region. Their geometrical variations were numerous, but a comprehensive mapping of performance was not done and the fundamental diffuser physics were not identified. Howell [6] provided a more detailed set of measurements of diffuser performance and an investigation of

ground-simulation methods. His measurements were similar to some of those reported here, but without the associated surface pressures and lacking an interpretation of the vehicle flowfield.

It is known that the performance of conventional diffusers in other applications can be collapsed onto non-dimensional maps [7,8] that correlate the basic performance parameter of pressure-recovery coefficient to diffuser geometry and inlet flow-area blockage. It is possible that automotive underbody diffusers have similar performance trends and that the lift and drag behaviours that result from them might collapse in a similar fashion.

OBJECTIVES

The primary objective of this investigation was to identify the physics of the underbody flows of road-vehicle-like bodies fitted with rear underbody diffusers. The approach taken was to select a simple underbody geometry to reduce complexity and to choose a body shape whose flowfield was only weakly interactive with changes in the underbody flows. This shape was similar to other generic automotive bodies used for basic aerodynamic research, and was also amenable to CFD analysis.

An additional goal was to quantify and explain the interaction of the underbody flow with the simulated groundboundary condition in order to give guidance in the choice of optimum simulation.

Finally, a database was acquired to provide insight into the drag- and lift-producing potentials of automotive underbody diffusers.

AERODYNAMIC MECHANISMS

The following sections offer a view of downforce generation and the role of the diffuser in it. The concepts discussed were the motivation for the experimental program and the analysis of its being reported here.

DOWNFORCE GENERATION – It is known that a diffuser in ground effect affects the drag of a vehicle and can produce high levels of downforce. There has been little published on the mechanisms that produce this downforce. Sovran, at the Pinninfarina Workshop in 1994 [9] presented the concept of the diffuser acting as a pump in the underbody flow path. This concept was intriguing and the test program reported in this paper was, in part, designed for its investigation.

As the project progressed, it was realised that several other identifiable fluid-mechanical mechanisms were also at work. It is therefore useful to describe them at the outset so that they can be used as the basis for analysing and understanding the experimental results to be presented. One mechanism is 'ground interaction', a second is 'underbody upsweep' (body camber) and the third is the concept of 'diffuser pumping'.

<u>Upsweep</u> – The presence of upsweep on the rear underbody of an otherwise symmetrical body will camber the body, resulting in a downward-directed lift force, or downforce. The situation is exactly that of an inverted fastback automobile.

Ground Interaction – In potential flow, a symmetrical body in free air has zero lift. As the body is brought into ground proximity, flow asymmetry develops as the flow beneath the body accelerates due to ground constraint. The accompanying reduction in underbody static pressure produces downforce on the body. The downforce increases with increasing proximity to the ground, and approaches infinity as ground clearance (ride height) approaches zero. This behaviour is shown schematically in Figure 1.

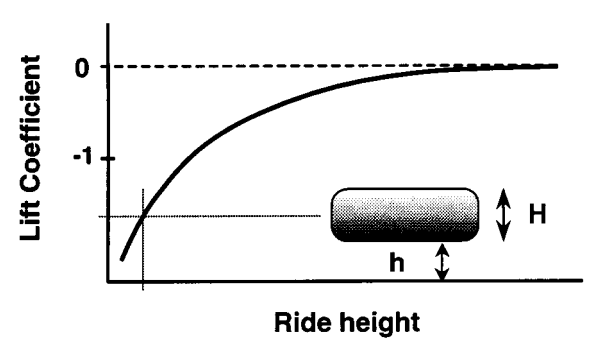
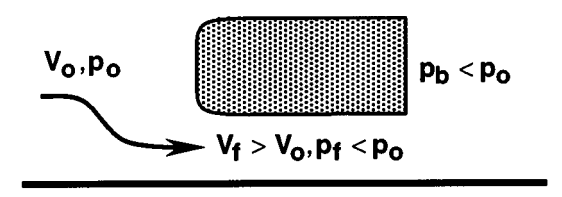


Figure 1. Schematic of Potential-flow Downforce Behaviour

Real flows, however, are not inviscid. The effects of fluid viscosity on the underbody flow are minimal at large ride height, but become increasingly significant as ride height is reduced, eventually becoming dominant and terminating the increase in downforce at some small value of ride height.

<u>Diffuser Pumping</u> – A subsonic diffuser is an internal-flow device whose cross-sectional area increases in the flow direction, producing a decrease in fluid velocity from inlet to outlet, with a corresponding increase in static pressure. This pressure rise can be used to increase the flow rate through a system, as was known even in Roman times.

When a diffuser delivers flow to a fixed exit pressure - the base pressure of an automobile as an example - its pressure recovery appears as a depression in pressure at the diffuser inlet. This concept is illustrated in Figure 2 for a flat-bottomed and a diffuser-equipped model. There is downforce on the flat-bottomed model, but the presence of the diffuser in the bottom drawing reduces the underbody pressures further. That configuration will have the greater underbody flow rate, lower underbody pressure and the greater downforce. The diffuser can be considered to have 'pumped-down' the underbody, inducing a component of downward force on the vehicle.



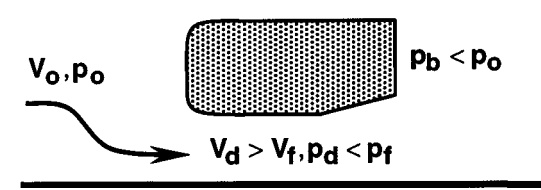


Figure 2. The Underbody Diffuser

The pressure rise in the diffuser drives this process, so it is the pressure-recovery behaviour of the diffuser that should govern its influence on an automobile. This pressure rise is a function of the ratio of the areas at the outlet and the inlet of the diffuser, where this area ratio is set by the diffuser angle and the vehicle ride height.

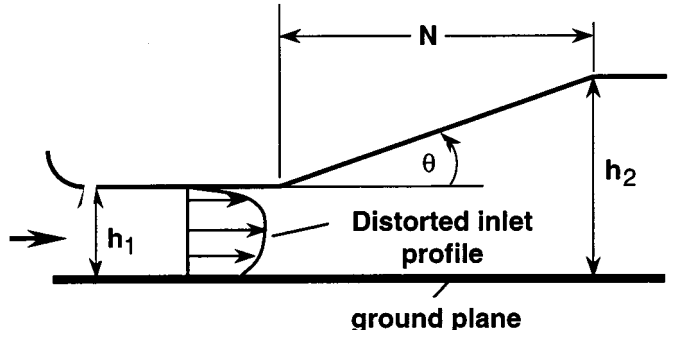


Figure 3. Schematic of Diffuser Geometry

DIFFUSER FUNDAMENTALS

Diffuser pressure recovery is the performance parameter of major interest in diffuser design. The definition of the pressure-recovery coefficient and of the other important diffuser geometric parameters are now presented, followed by a summary of typical diffuser performance characteristics as a guide to the expected form of diffuser behaviour in an automotive application.

DIFFUSER GEOMETRY – The automotive diffuser is sketched in Figure 3 and it is seen to be asymmetric. This asymmetry is a minor factor in the performance of the diffuser.

DEFINITIONS OF PARAMETERS – The pressure-recovery coefficient of a diffuser is defined as,

$$\overline{C}_p = \frac{(p_2 - p_1)}{1/2p\overline{U}_1^{-2}}$$
 (Eq. 1)

where \overline{U}_1 is the area-average inlet velocity, p_1 is the diffuser inlet static pressure and p_2 is the static pressure at the exit plane of the diffuser.

The ideal pressure-recovery coefficient, the value provided by full expansion of a one-dimensional flow with no internal losses, is,

$$C_{pi} = 1 - \frac{1}{AR^2}$$
 (Eq. 2)

where the area ratio is $AR = (A_2 / A_1) = (h_2 / h_1)$. The diffuser effectiveness is the ratio of equation (1) divided by equation (2), that is, the fraction of the ideal pressure recovery that is produced at a given area ratio. As such, it is a measure of the amount of flow expansion that is actually experienced.

The area ratio of the asymmetric geometry of Figure 4 can be expressed as,

$$AR = 1 + \left(\frac{N}{h_1}\right) \tan \theta$$
 (Eq. 3)

This expression presents the interrelationship between the geometric parameters of the diffuser. It can be seen from this that a vehicle with large ride height will have a smaller area ratio at a given diffuser angle than the same diffuser at a lower ride height. At a given ride height, the area ratio may be increased by increasing diffuser angle.

NON-DIMENSIONAL DIFFUSER PARAMETERS – The important geometric parameters governing diffuser performance are the inlet and outlet area, diffuser length, and inlet velocity profile. The geometric variables can be grouped into three non-dimensional parameters of primary importance - area ratio, inlet aspect ratio and non-dimensional diffuser length. Restricting the study to two-dimensional (or quasi-two-dimensional) diffusers, aspect ratio is excluded, and the geometry can be described in terms of any two of:

$$(h_2/h_1), (N/h_1), \theta$$

where the first term is the area ratio of the single-expansion diffuser, the second is its non-dimensional length and the third is the diffuser angle. These three parameters are related through equation (3).

The length and the roughness of the entry section beneath the vehicle upstream of the diffuser inlet are other parameters of importance since they determine its inlet flow conditions. The underbody was smooth in this test and the data are reported for only one underbody length, so length parameters are not evaluated in this paper.

TWO-DIMENSIONAL DIFFUSER PERFORMANCE – Sovran & Klomp [7] and Reneau, Johnston & Kline [8] have mapped diffuser performance on the basis of area ratio and non-dimensional length, as shown in Figure 4.

This Figure depicts the pressure recovery of symmetric two-dimensional, plane-wall, single-expansion diffusers as a function of the primary, non-dimensional geometric parameters. A constant diffuser angle appears as a straight line radiating from the origin.

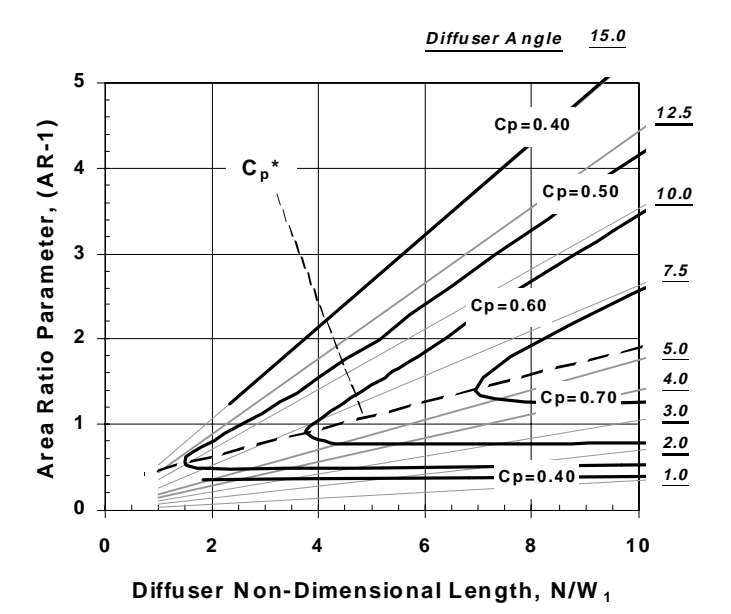


Figure 4. Contours of Constant Pressure-Recovery

Coefficient for a Two-dimensional Diffuser [7]

The contours of constant pressure-recovery coefficient (bold lines) show a characteristic form that defines a locus of optimum pressure recovery that lies along the knees in the contours. This locus defines the diffuser area ratio producing maximum pressure recovery for a given non-dimensional diffuser length. Sovran & Klomp [7] have termed this locus the C_p line.

It was hoped that the performance of underbody diffusers would follow a similar characteristic. As the diffuser geometry on an automobile is varied, its pressure recovery might vary in a fashion that is qualitatively similar to that exhibited in Figure 5. It is anticipated that the strength of the underbody flow will reflect pressure-recovery behaviour, as will the downforce and the drag produced. How similar the automotive situation might be to the two-dimensional case with end walls is one of the issues to be examined in this study.

DIFFUSER INLET BLOCKAGE – It is known that a non-uniform velocity profile across a diffuser inlet becomes increasingly distorted as the flow experiences the positive pressure gradient in the diffuser. Since a distorted velocity profile effectively blocks part of the flow cross-section, the result is an effective reduction in the area ratio of the diffuser and a reduction in its pressure rise.

Sovran & Klomp [7] have introduced the blocked-area fraction of an internal flow, defined by them as,

$$B = \frac{1}{A} \int_{0}^{A} \left(1 - \frac{u}{U} \right) da$$
 (Eq. 4)

where u is the local velocity in a cross section A, and U its maximum value. Furthermore, they have quantified how diffuser inlet blockage B₁ reduces the pressure recovery of optimum diffusers.

For the two-dimensional diffuser with an in-flow consisting of a uniform-velocity core bounded by boundary lay ers, B_1 is the ratio of the sum of the displacement thicknesses on the two walls of the inlet channel to the inlet height,

$$B_1 = \frac{(\delta_a^* + \delta_b^*)}{h_1}$$
 (Eq. 5)

AUTOMOTIVE APPLICATION – It is anticipated that an automotive diffuser, even at the high aspect ratios found for low-underbody-clearance racing cars, will be influenced by three-dimensional flow effects, except in the case where the sides of the underbody are sealed to the ground, as in the case of now-illegal, skirted racing cars. George & Donis [5] showed clearly that strong vortices are produced near the side edges of the diffuser due to the induced inflow. Nevertheless, the diffuser performance map that has been presented might govern the qualitative behaviour.

EFFECTS OF GROUND SIMULATION

It is generally accepted that a moving ground is required for accurate wind-tunnel simulation of racing cars. Until recently, it was accepted that a fixed ground was adequate for road-vehicle development. However, as technology and knowledge evolve, these presumptions should be, and are being, revisited. Several recent studies [3,4,10,11] have explored this issue.

Full-width belt systems that are wider than an automobile usually carry the rotating wheels on outriggers; consequently, wheel lift is not measured. Such systems provide the best conditions for underbody development but leave some uncertainty because changes to the body must influence wheel lift.

Narrow belt systems, where the belt just runs between the tires, have been studied and appear to be a promising compromise, although their limitations are not fully understood [10,11].

A general survey of the current status of ground-simulation issues was made at a workshop sponsored by Pininfarina and the National Research Council (CNR) of Italy in 1994. In one paper, Cooper [12] used data provided by Carr [13] to summarise the effects of several ground-simulation techniques. This summary is presented in Figure 5.

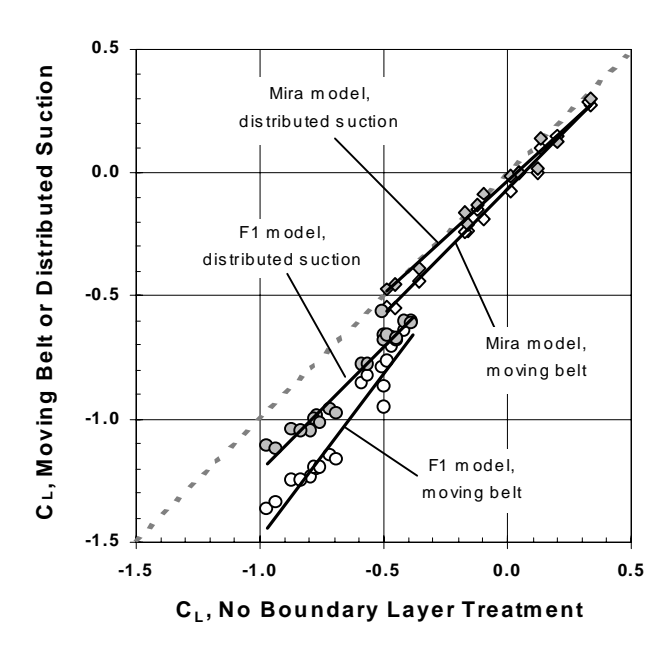


Figure 5. Effect of Ground Simulation on Downforce [13,15]

The data are for a simplified passenger-car model (the MIRA model) and for a fairly detailed Formula 1 racing-car model. It can be seen for the passenger car that the fixed-floor ground simulation produces nearly the same result as the moving-belt or distributed-suction ground simulations. However, for the racing car with an underbody diffuser, the fixed floor is inadequate, giving downforce that is less than with either the moving-belt or the distributed-suction ground simulations.

Recent studies by Mercker & Wiedemann [4], Cooper, Fediw, Garry & Wlodarski [10], Cogotti [14] and Carr [11] provide conflicting views of the wide and narrow-belt effects. The end result is that the issue of whether moving belts, either wide or narrow, are necessary for passenger-car studies is still unresolved.

WIND TUNNEL TEST DESCRIPTION

A simple rectangular-block model with rounded leading edges was fitted with underbody diffusers of two lengths for the present investigation. These diffusers had adjustable angles and were fitted with endplates. The two diffuser lengths were typical of those that might be fitted to road or racing vehicles. The model was attached to an overhead carriage by a streamlined strut that permitted the ride height, and thereby the diffuser area ratio, to be quickly varied over a wide range. This assembly was positioned over a moving belt system in the NRC 0.9m x 0.9 m Pilot Wind Tunnel.

The primary geometric parameters that govern underbody flows were varied to cover the range of interest by testing two diffuser lengths of variable wall angle over a range of ride heights. The ground simulation was varied from fixed with no blowing, through fixed floor with tangential blowing, to the ideal case of moving floor with tangential blowing. These simulations spanned the range of

those commonly used and were selected to help improve our understanding of the flow interactions at the ride heights of automotive interest.

MODEL – The model had a length of 396.2 mm, a width of 212.3 mm and a height of 165.1 mm (l:w:h=2.40:1.30:1.00). The frontal area was 0.0351 m2. The four circular-arc leading edges had radii of 34 mm, giving $r/\sqrt{S}=0.18$, where S is the frontal area of the body. The model width was 24 percent of the width of the belt and its length was 26 percent of the belt length. The model is shown in the drawing of Figure 6 and the photograph of Figure 7.

The model was fitted with diffusers that were 25% and 75% of the length of the model, 97.8 mm and 297.8 mm, respectively. The angle of each diffuser could be adjusted from 0° to more than 15°. The diffusers were fitted with endplates for most of the study, and nearly all of the measurements were made at zero pitch angle. A few runs were made with non-zero pitch angle and with the endplates removed.

A circumferential distribution of surface-pressure taps was positioned on or near the longitudinal centre plane of the model at the locations shown in Figure 6. The taps on the front face and underneath the model were positioned on the centre line, while the row of taps on the top of the model was displaced 38 mm laterally to clear the mounting strut. The base pressure taps on the vertical rear face were connected together and averaged pneumatically to give the average base pressure over the full base area. The number of rows of taps averaged this way varied with the diffuser angle. Two other sets of taps on the top of the model, marked by curly parentheses in Figure 6, were averaged in the same fashion. The pressure measurements were made by a Scanivalve ZOC-23B, 2.5 kPa, 32-port scanner.

Aeroynamic forces were measured by a JR3 six-component, strain-gauge balance mounted inside the model. The balance had load ranges of +222 N in lift, +111 N drag and +8.5 N-m in pitching moment. It had a measuring accuracy of 0.5%.

The measurements were made at a speed of 30 m/s, giving a model-length-based Reynolds number of 8.3×10^5 . The diffuser Reynolds number at the 25 mm ride height, based on the average underbody velocity and the model ride height, was approximately 5×10^4 , which is just on the boundary above which Reynolds number should not affect diffuser behaviour. At the lower ride heights this Reynolds number will be reduced and some Reynolds-number effects might be expected. A higher speed was not used because the belt system would not run faster than this with high levels of suction on the belt to stop it from lifting under the model.

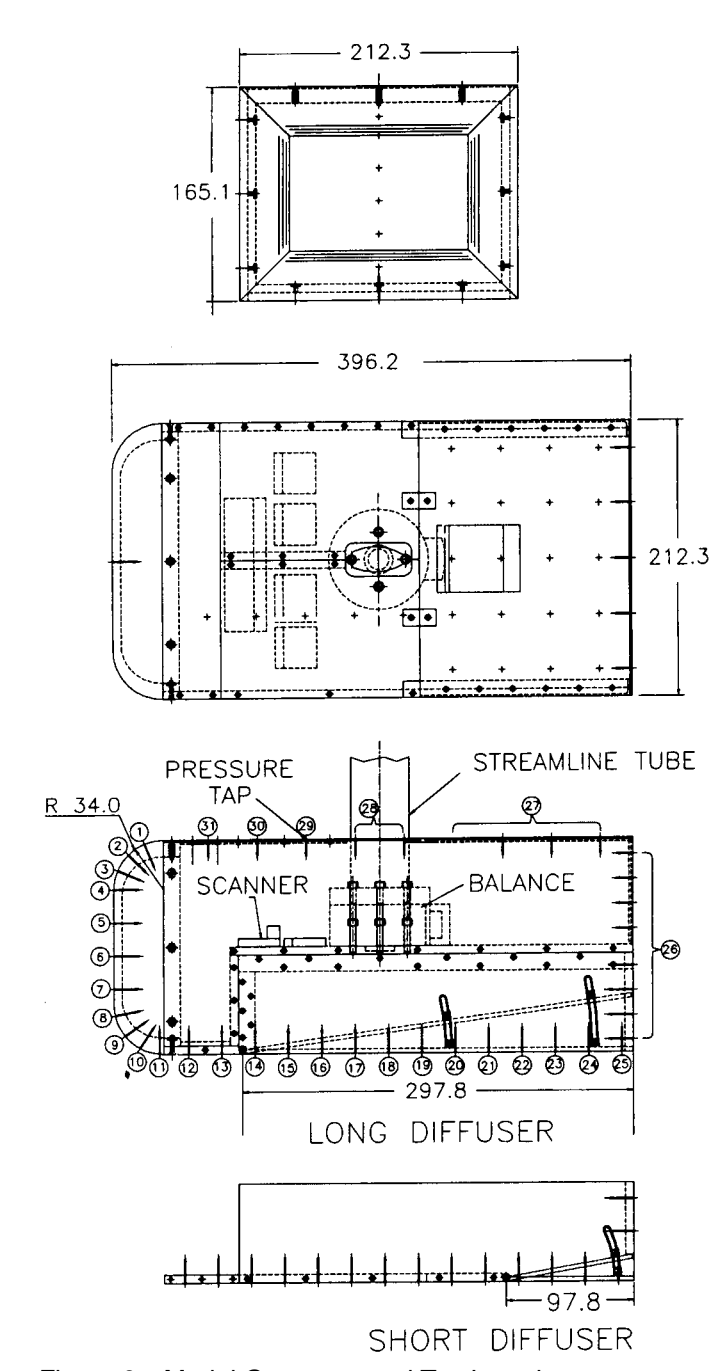


Figure 6. Model Geometry and Tap Locations

WIND TUNNEL INSTALLATION – The Pilot Wind Tunnel is a 1:10-scale model of the NRCC 9m x 9m wind tunnel. It is used for tunnel development and fundamental research. It is equipped with a moving-belt system to permit research into ground effects.

<u>Tunnel Characteristics</u> – The wind tunnel is a horizontal-circuit, closed-wall, closed-return, atmospheric facility with a contraction ratio of 6 and two turbulence screens. The test section is 914 mm high, 914 mm wide and 2286 mm long. The tunnel turbulence level is 0.5 percent and the mean-velocity profile is constant within 0.7 percent of the average value across the test section. The maximum air speed is 55 m/s.

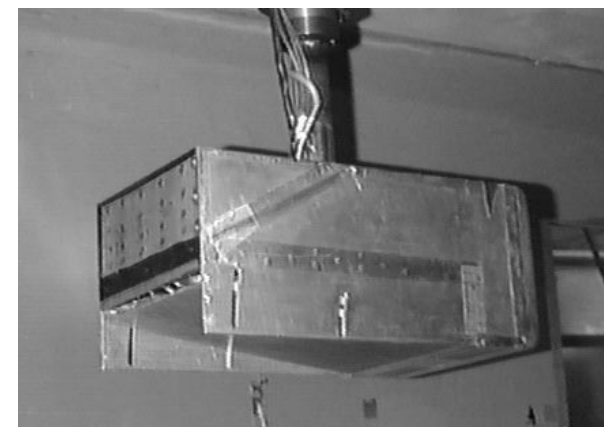


Figure 7. Long Diffuser Showing the Endplates

Model Mounting Strut and Balance Assembly — The model was connected through the internal, strain-gauge balance to an overhead, streamlined, vertical strut. This strut was attached to a computer-controlled traversing system that accurately positioned the model above the belt. The strut had a universal joint that allowed the model yaw, pitch and roll attitudes to be set manually. The traversing system was mounted to an overhead beam structure connected to the foundations of the building to avoid any balance excitation due to vibrations of the floor.

Moving-belt System – The tunnel was equipped with a four-roller moving-belt system driven by a 19 kW hydraulic motor . The belt is 900 mm wide and 1525 mm long. The two upper rollers establish the working surface, which is supported by a 15-mm thick, hard-coated aluminium plate. The plate has two suction plenae that keep the belt from lifting as the belt leaves the front drive roller and passes through the low-pressure region beneath the model.

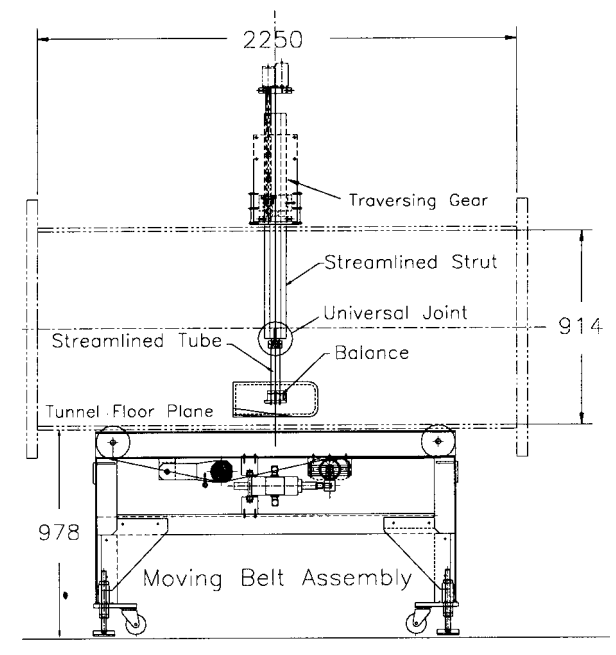


Figure 8. Moving-belt Installation in the Pilot Wind Tunnel

The front lower roller steers the belt, using an array of LED light sources and optical sensors connected to a PID controller. The controller drives an hydraulic actuator that pivots the steering roller in the horizontal plane about one end to provide the steering force. The rear lower roller is spring-loaded, to set belt tension. The belt speed controller maintains set speed within . The maximum belt speed is 35 m/s with suction on. The wind tunnel and belt system are shown in the drawing of Figure 8 and the photograph of Figure 9.

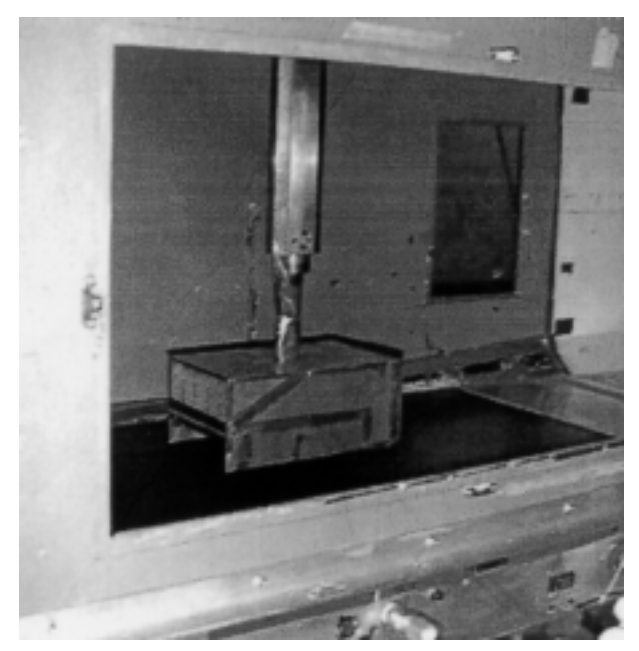


Figure 9. Wind Tunnel Installation Showing Model, Mounting Strut and Moving-belt System

TEST PROGRAM

TEST MATRIX – The primary purpose of the test program was to evaluate the behaviour of underbody diffusers as functions of diffuser length, diffuser angle and area ratio. The test points were chosen to provide a sufficiently dense array of data points that contour plots of lift, drag and pressure recovery could be prepared in the same format as the classical two-dimensional diffuser pressure-recovery plots of Figure 4.

In addition to the main matrix of nine diffuser angles and 22 ride heights, each length diffuser was tested at one diffuser angle - 9.17 degrees for the short diffuser and 12.91 degrees for the long diffuser - with the diffuser end-plates removed. Finally, each diffuser was tested near its optimum diffuser angle at three non-zero pitch angles. The angles for the short diffuser were +1.57 degrees, -1.60 degrees and -2.75 degrees.

While ride height and diffuser angle were the parameters that were varied experimentally, it is important to note that both affect area ratio. As ride height decreases or diffuser angle increases, the area ratio of the diffuser increases.

TEST PROCEDURE – The model was run through the full test matrix (diffuser length, diffuser angle, ride height) for each of the three ground boundary conditions. For each run, diffuser angle and length were fixed, the data system zeros were read, and the tunnel was accelerated to its operating speed of 30 m/s. The ground condition was set and a complete set of ride heights were run under computer control of the traversing system. The tunnel was stopped, the zeros on the data system were reset, the next boundary condition was established and the process repeated. Several repeat measurements were made after complete removal and reinstallation of the model to verify system repeatability.

At each measurement point, lift, drag and pitching moment were measured and the pressure taps were scanned. Due to model symmetry the other three force and moment components were zero and were not recorded.

FLOOR BOUNDARY LAYER - The floor boundary layers were measured for each of the ground simulations to establish the boundary-layer displacement thickness and to determine the blowing pressures required. The measurements were made with an array of total-pressure tubes that extended across the width occupied by the model. The vertical positioning was provided by the traversing system. The average profiles across the model width were used to define the boundary layer profiles. The displacement thickness on the fixed floor was 5.44 mm. The displacement thickness with the floor fixed or moving could be adjusted by varying the blowing-plenum supply pressure. A series of blowing-plenum pressures were tried to examine the boundary layer changes, and a cross-plot of the resulting displacement thicknesses versus pressure allowed the required plenum pressure to be selected. Figure 10 shows the variation of the meanvelocity profiles with height for the fixed ground and the moving ground. It was possible to produce negative displacement thickness by over-blowing.

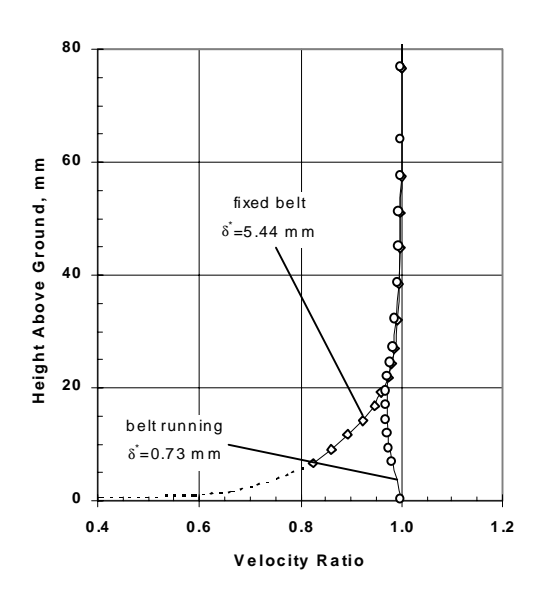


Figure 10. Floor Boundary-layer Profiles

The blowing pressure was chosen to be 35.2 kPa with the belt running, leaving a displacement thickness of 0.8 mm and no super-velocity in the profile, that is, no velocity above free-stream value.

DATA REDUCTION – The forces, moments and pressures were reduced to coefficient form using standard definitions. The wind tunnel was calibrated for each ground simulation. The appropriate dynamic pressure calibrations and static-pressure offsets were used in the data reduction.

The uncorrected force and pressure coefficients are defined as:

drag

$$C_{D} = \frac{D}{qS}$$
 (Eq. 6)

lift

$$C_{L} = \frac{L}{qS}$$
 (Eq. 7)

pressure

$$C_{p} = \frac{(p - p_{\infty})}{q} + \Delta C_{p}$$
 (Eq. 8)

where D is drag, L is lift, S is the reference frontal area, p is surface pressure, p_{∞} is the upstream reference static pressure, q is calibrated, blockage-uncorrected, tunnel dynamic pressure and ΔC_p is the offset pressure coefficient between the static-reference taps and the model location. The coordinate origin was taken at the model centre, at ground level.

The data were corrected for blockage using a modified version of the correction of Thom and Herriot [16]. The correction included a drag increment due to wake constraint. The blockage correction varied with height, due to the change in mounting-strut length. The correction was typically 6 percent of dynamic pressure. The corrections were applied in the following fashion,

$$C_{Dc} = \frac{(C_D + \Delta C_{Dwi})}{(q_c / q)}$$
 (Eq. 9)

$$C_{Lc} = \frac{C_L}{(q_c/q)}$$
 (Eq. 10)

$$C_{pc} = 1 - \frac{(1 - C_p)}{(q_c / q)}$$
 (Eq. 11)

where, (q_c / q) is the blockage correction factor and ΔC_{Dwi} = -(1/4)C $_{Du}^2$ (S/C) is the drag increment due to wake constraint.

NUMERICAL SIMULATION

Several of the test cases were simulated numerically. A three-dimensional CFD model was used to detail the flowfield as an aid in the interpretation of diffuser behaviour. The computations used the commercial flow solver CFD-ACE. This solver uses a finite-volume approach on a structured, multi-block, body-fitted-coordinate grid. CFD-ACE is a pressure-based flow solver using the SIM-PLEC pressure-correction algorithm.

The convective terms in the governing equations were discretised using a second-order upwind scheme, with a blending of first-order to maintain solver stability. CFD-ACE offers a variety of turbulence models. Due to the possibility of flow separation in the diffuser, the k-w model (with integration of the governing equations to the wall) was chosen for this application.

The flow was assumed to be fully turbulent, as no tools exist in the flow solver for dealing with transition. The grid was generated using CFD-GEOM. Due to symmetry, only the half-model was gridded using a C-O topology blended into a background H-mesh to accommodate the ground plane. The algebraic grid generated a near-wall spacing that maintained y+ values less than unity, with approximately 25 points both in the boundary layer on the body and on the ground plane. The total number of grid points was 676,000.

Two different boundary conditions were applied to the ground plane. The first simulated that of a moving floor, with the floor treated as a no-slip surface moving at the free-stream velocity of 30m/s. The second condition was that of a stationary, no-slip wall. The upstream, uniform-inlet-velocity boundary was located at a point sufficiently far upstream of the model to generate a boundary layer thickness close to that measured in the empty test section. The computations were performed on a Silicon Graphics Power Challenge containing six R8000 processors and 1.5GB of memory. A typical run time for one simulation was on the order of 96 hours.

PRESENTATION OF RESULTS

Only the force and pressure data measured for the model with short diffuser, and both fixed-ground and moving-ground simulations, are presented in this paper. This diffuser model was chosen because the relatively long underbody upstream of the start of the diffuser allows the front-end entry flow to be isolated from the diffuser flow. Again, the purpose is to examine the physics of diffuser-induced flows with as little extraneous influence as possible

The same reasoning excluded the fixed-floor, tangentialblowing ground simulation because each setting of the blowing pressure produced a different displacement thickness. The other two ground simulations - fixed-floor and moving-belt - are the bounding conditions on the flow and are unambiguous. One represents the classical wind-tunnel approach while the other is closer to the onroad condition.

FORCE MEASUREMENTS – The lift and drag measurements for the fixed-ground and moving-ground simulations are presented in Figures 11 to 14. The data are plotted against ride height non-dimensionalised by model height. Each graph contains a series of parametric plots of lift or drag, with diffuser angle as the parameter.

<u>Lift Measurements</u> – The lift measurements are presented in Figures 11 and 12 for the ground fixed and moving, respectively. The drag is presented for the same ground simulations in Figures 13 and 14, respectively. The following discussions use the fixed-ground case as the reference; it and the moving-ground data sets have similar behaviour.

The term downforce will be used to describe the magnitude of the negative lift coefficients, clarifying discussion by removing the confusion that may result from descriptions of 'increases in negative lift'.

Figure 11 shows that, for a fixed diffuser angle, as ride height decreases, downforce increases until a maximum is reached at a small value of ride height. Below this ride height, the downforce reduces rapidly. In potential flow, the downforce would not have a minimum. Therefore, the minimum must be the result of viscous effects that

become significant at low ride heights where it is assumed that the sum of the boundary layer thicknesses on the underbody and on the ground become a major fraction of the ride height.

At all ride heights above $(h_1/H) = 0.20$, the family of constant-diffuser-angle downforce curves form a nearly parallel family that show a monotonic increase in downforce with increasing diffuser angle, to the maximum tested. At ride heights below this value, the consistent trend in downforce is reversed for diffuser angles greater than 9.64 degrees. All the fixed-ground downforce curves and most of the moving-ground downforce curves show a sharp downforce reduction at the lowest ride heights of $(h_1/H) < 0.06$.

In general, the moving-ground simulation produces similar downforce magnitudes at large ride heights to those measured with the fixed-ground simulation, and increasingly larger downforce as the ground is approached. The differences in downforce are not large, being considerably smaller than those found for wheeled cars, as typified by Figure 5. The largest effects of ground simulation are observed for diffuser angles less than 9.64 degrees, at the lower ride heights.

A comparison of typical downforce levels for the fixed and the moving ground is made in Figure 15.

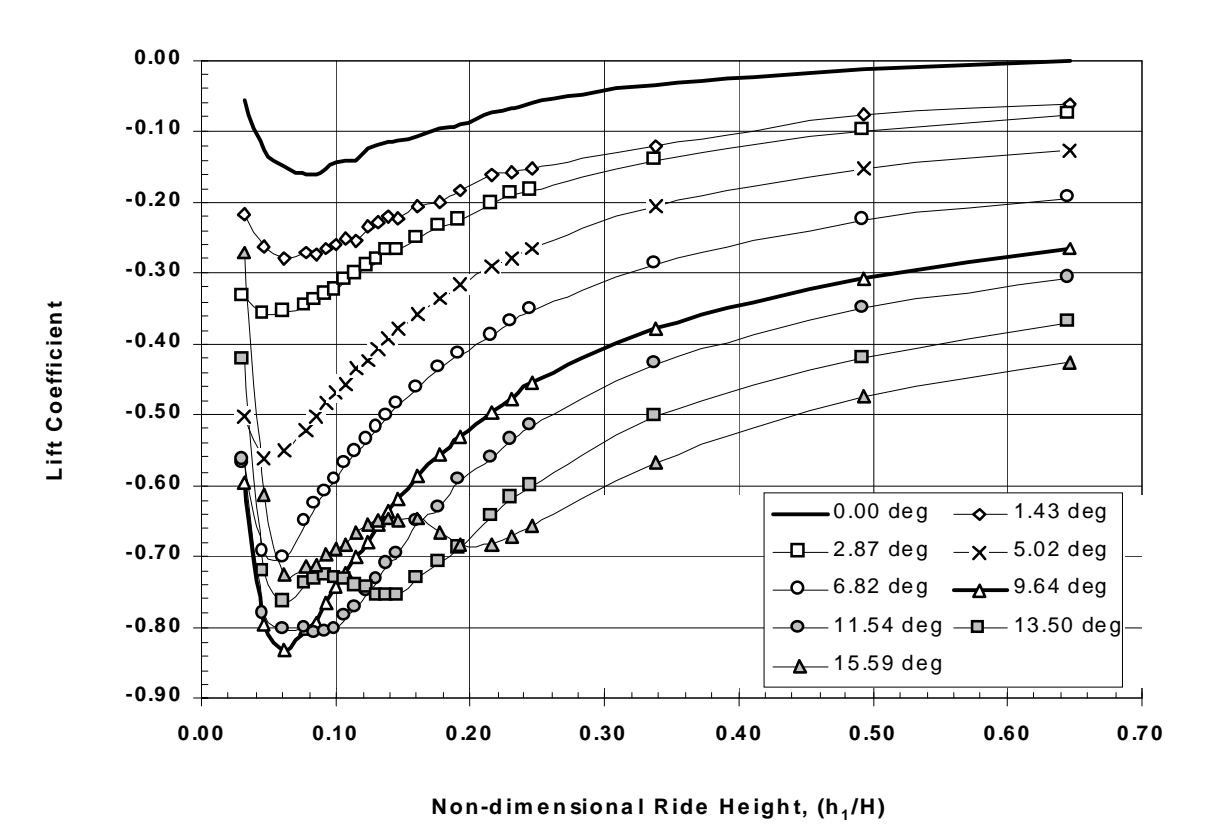


Figure 11. Measured Downforce for the Short Diffuser, Fixed Ground

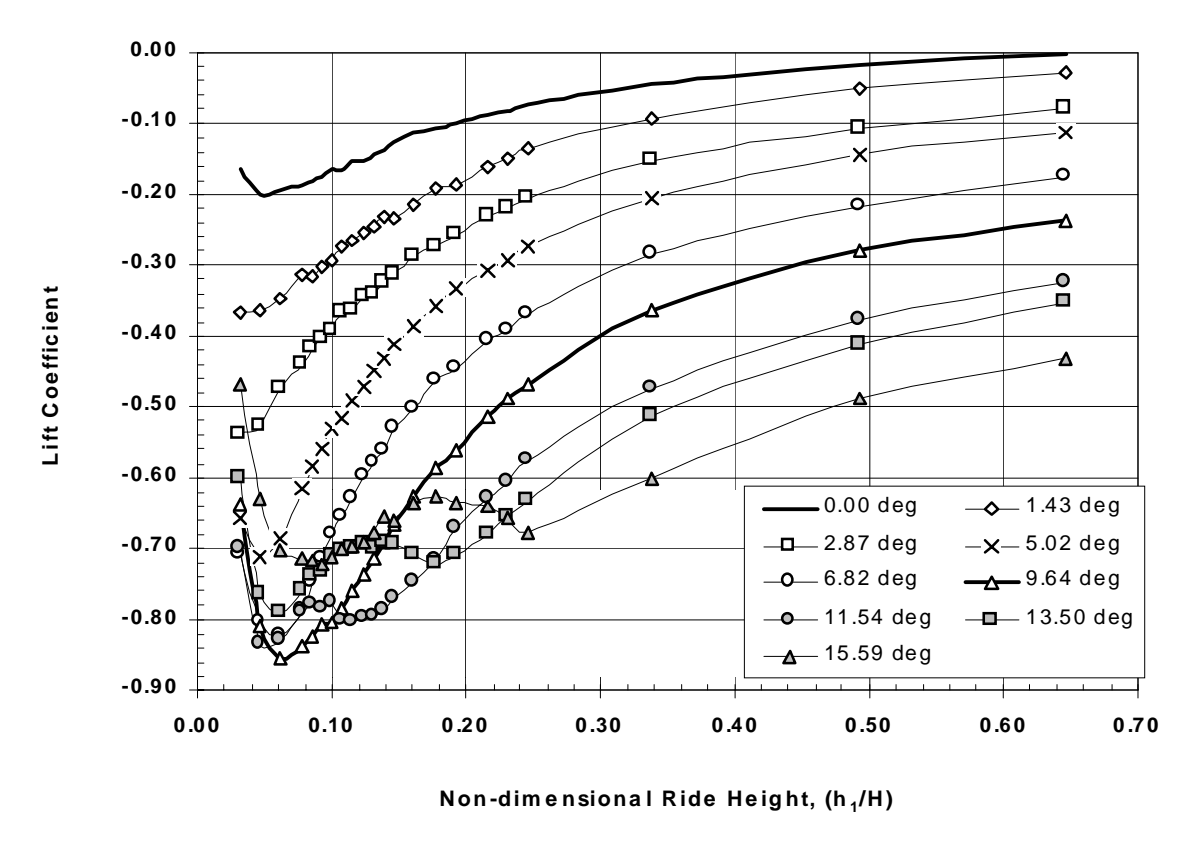


Figure 12. Measured Downforce for the Short Diffuser, Belt Running

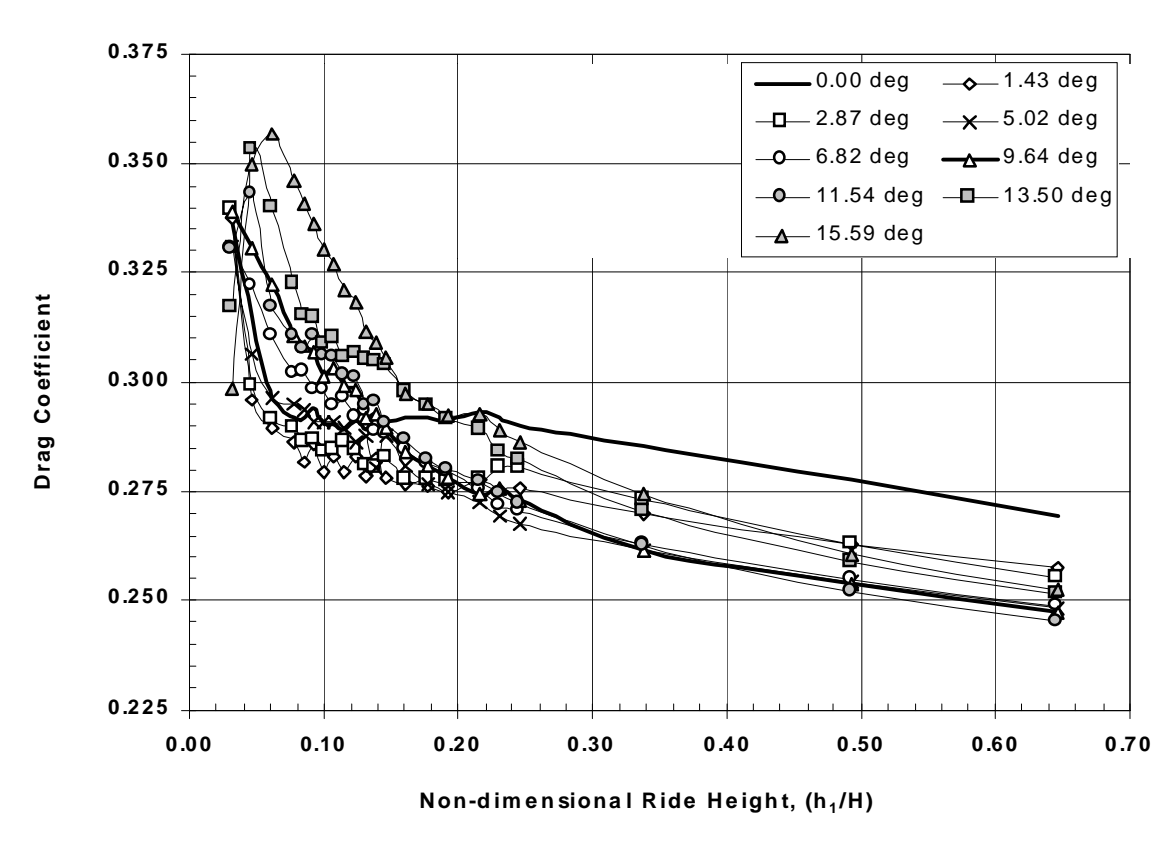


Figure 13. Measured Drag for the Short Diffuser, Fixed Ground

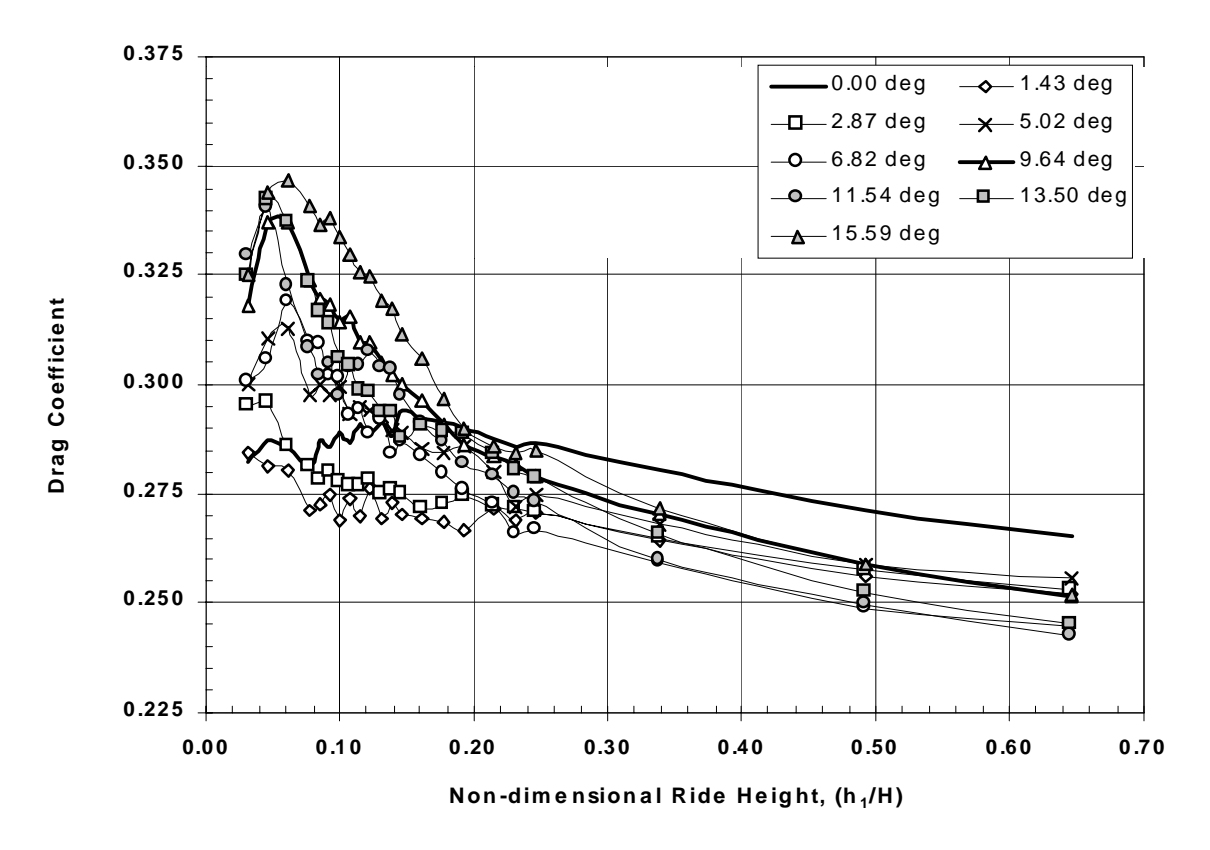


Figure 14. Measured Drag for the Short Diffuser, Belt Running

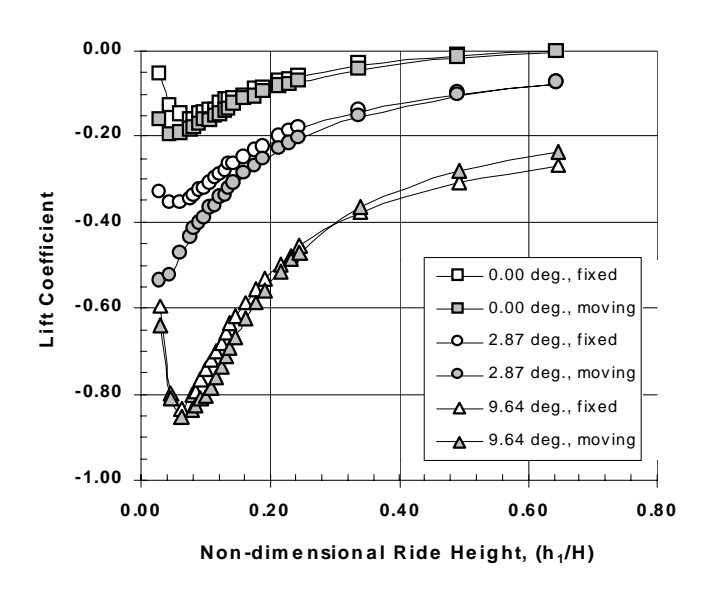


Figure 15. Comparison of Downforce with Fixed-ground and Moving-ground Simulations

<u>Drag Measurements</u> – Drag shows a more complex behaviour than downforce. The most obvious trend is that drag is reduced by underbody upsweep at large ride heights, and increased by the corresponding diffuser at low ride heights. The ride heights at which the drag increase begins is essentially the ride-height region over which the downforce increases rapidly. The transition to increased drag can be seen through a comparison of the

bold lines at zero diffuser angle in Figures 13 and 14 with the surrounding data at non-zero angle.

The general form of all drag curves is a monotonic drag increase with reducing ride height down to (h_1 / H) =0.062 for both ground simulations. Below this ride height the ground simulations differ. With the ground fixed, the drag continues to increase for diffuser angles at or below 9.64 degrees. With the moving ground at all diffuser angles but the smallest, and for the fixed ground above 9.64 degrees, the drag decreases for (h_1 / H) <0.062.

Most intriguing is the large difference in drag between the fixed-ground and the moving-ground simulations at these low ride heights for the zero-angle diffuser. This behaviour is seen more clearly in Figure 16.

A rapid drag rise occurs with the fixed-ground simulation at (h_1/H) <0.062 that is not seen with the moving ground. A similar difference was not observed in the lift behaviour between the two ground simulations. However, it is the same ride-height region over which the downforce for both ground simulations decreases rapidly. The drag increase may result from an increase in skin friction over the flat underbody at low ride heights when the ground is not moving. This drag behaviour marks a clear difference between the fixed-ground and moving-ground simulations, and the ride heights below which it appears will be termed the 'viscous ground effects' region.

The behaviour is not a measurement error because an identical result was found for the long diffuser at zero angle.

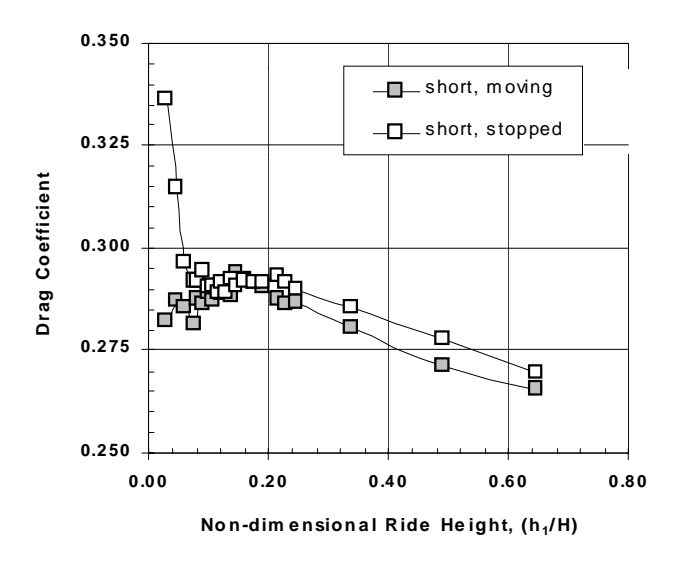


Figure 16. Effect of Ground Simulation on Drag at Zero Diffuser Angle

PRESSURE MEASUREMENTS

The trends in the data presented show consistencies that suggest well organised flow physics. Families of such well-ordered lift and drag curves also suggest the possibility of data collapse, which would provide insight into the phenomena involved and permit more general interpretation of the data. The following sections will expose some of these phenomena and will provide a framework for the analysis and understanding of the effects of underbody diffusers on surface-vehicle aerodynamics.

PRESSURE DISTRIBUTIONS – The centre-line pressure distributions that were measured provide insight into the force mechanisms at work. The introductory summaries of the force measurements have demonstrated that the diffuser is effective in generating downforce. At low downforce levels the diffuser can also provide a drag reduction, while at high downforce levels it always increases drag. The pressure distributions will allow this process to be examined in some detail.

Figure 17 presents a typical set of pressure distributions for the set of 22 ride heights. They are at a diffuser angle of 9.64 degrees with the ground moving.

Starting from the left, the upper-edge suctions are plotted first. These suctions increase slightly as the ride height is decreased. Next follows a characteristic front-face distribution, which peaks at a pressure coefficient near unity. The stagnation point moves downward with decreasing ride height. The flow accelerates around the lower edge, producing negative pressures in the vicinity of taps 8 through 11. These pressures increase slightly with reducing ride height. The underbody and diffuser pressures become increasingly negative at reduced ride height. This is a result of the increased pressure rise produced by increased area ratio due to ride-height reduction. The base pressure, tap 26, is nearly constant, as are the flat-upper-surface pressures.

The small bump in pressure at tap 12 in Figure 17 suggests the presence of a small, probably laminar, separation bubble at large ride heights in the adverse pressure gradient at the downstream end of the leading-edge radius. This bubble disappears at lower ride heights where the pressure gradient is reduced by ground proximity. The bubble is also present with the ground fixed, and the overall pressure patterns with fixed ground only differ in detail from those of Figure 17.

Figure 17 is useful for understanding the pressure field. However, the pressure distributions in Figures 18 and 19 for variable ride height and diffuser angle, respectively, allow better discrimination of detail.

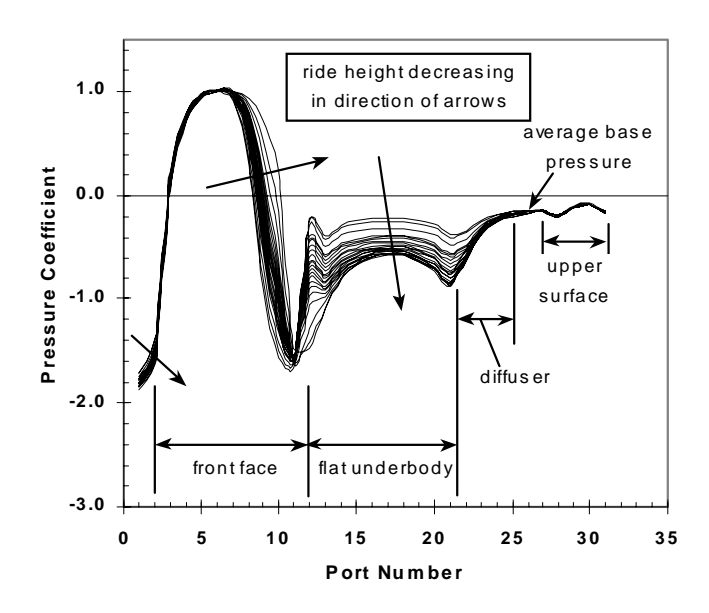


Figure 17. Typical Pressure Distributions with Ride Height as Parameter - Belt Running, θ =9.64°

Figure 18 shows the pressure distributions for the same case as Figure 17, but with fixed ground. The curves are qualitatively the same, with relatively small quantitative differences. The increasing pressure rise of the diffuser and the growing ground interaction with the lower forebody at reduced ride height are seen to propagate under the flat underbody. Both effects tend to produce a fairly uniform pressure decrease over the flat part of the underbody

Figure 19 summarises the effect of diffuser-angle changes on the pressure field at fixed height. The pressure field behaves quite differently than in Figure 18, with most of the pressure changes concentrated near the diffuser inlet due to increasing diffuser pressure recovery as diffuser angle is increased. There is no change on the forebody in this case.

A comparison of Figures 18 and 19 indicates that diffuser pressure rise dominates the rear half of the underbody, while ground interaction influences the front half due to the lower stagnation point increasing leading-edge flow acceleration as ride height is reduced.

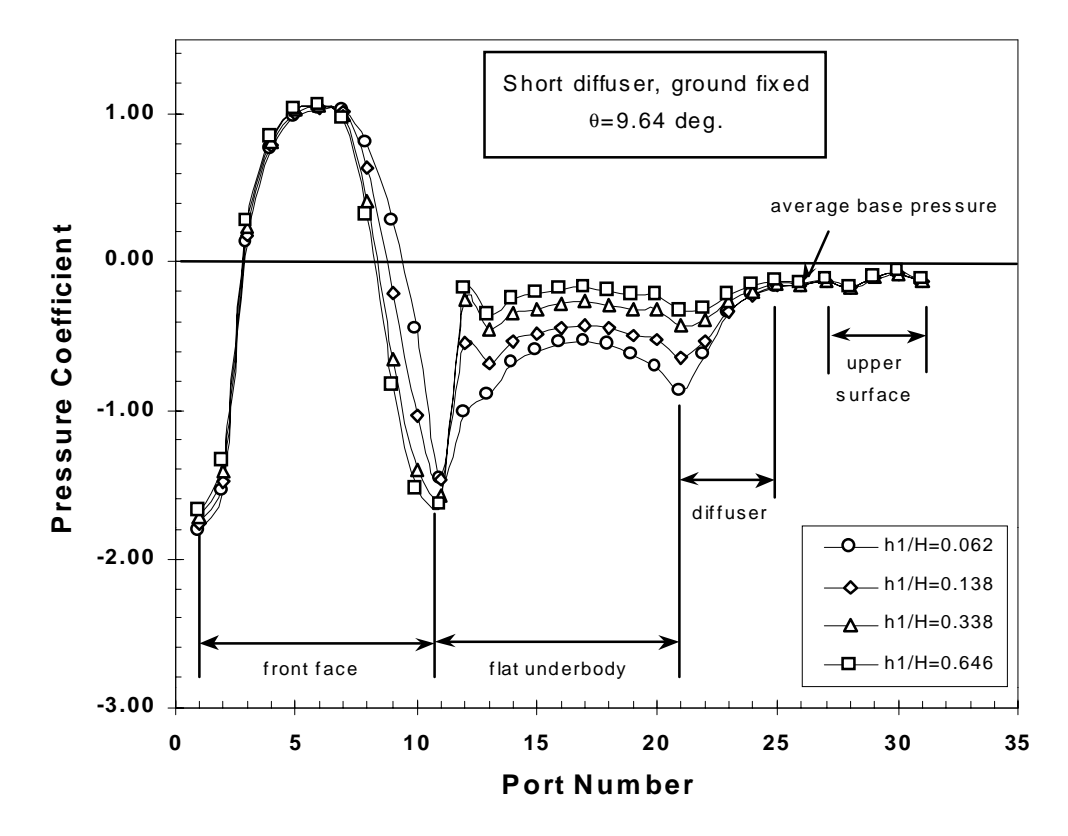


Figure 18. Typical Pressure Distributions with Ride Height as Parameter - Fixed Ground, θ =9.64°

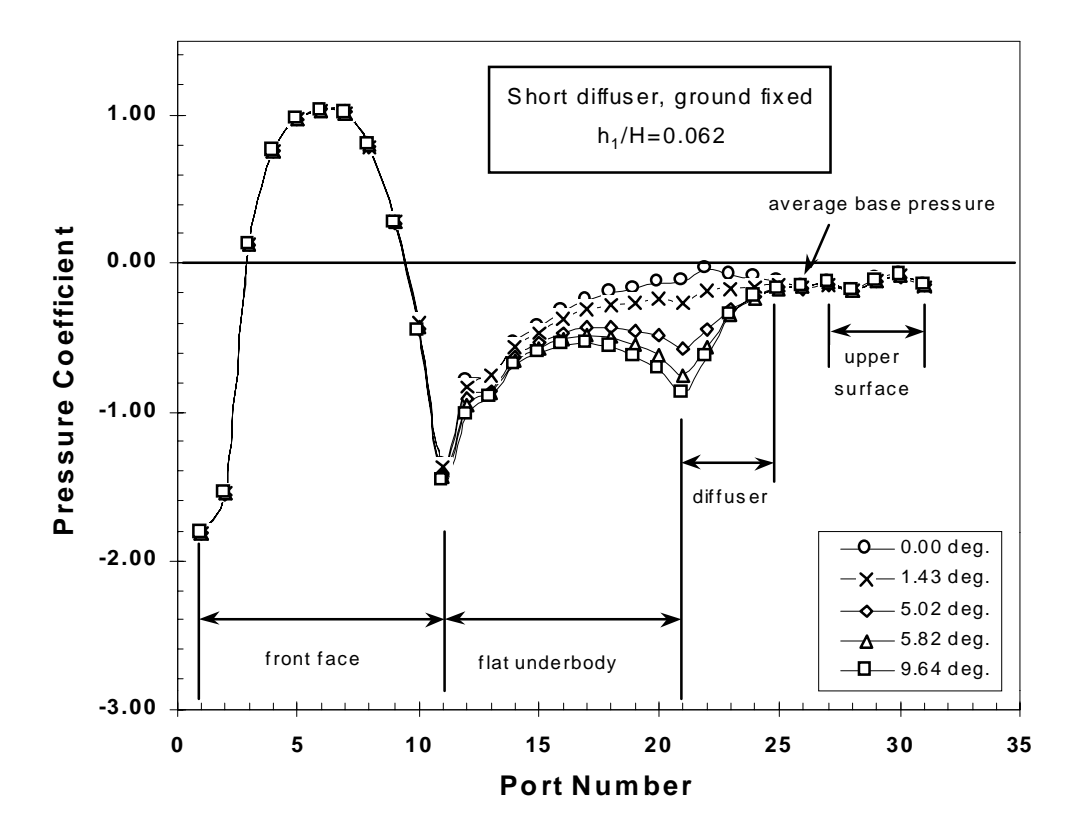


Figure 19. Typical Pressure Distributions with Diffuser Angle as Parameter - Fixed Ground, $(h_1/H)=0.062$

The effect of ground simulation can be seen in Figure 20. Compared to the fixed-ground case, small reductions in pressure occur along the upstream one-half of the flat underbody with the moving ground, with little change apparent over the diffuser. These modest pressure reductions are in line with the small increases in downforce with the moving ground.

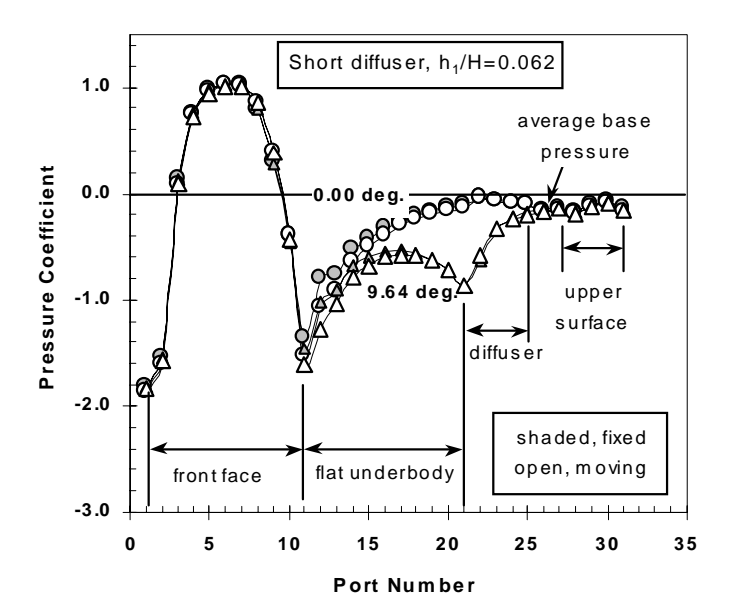


Figure 20. Effect of Fixed and Moving Ground Simulation on Surface Pressure

When ride height is reduced, a close examination of the front-face pressures in the vicinity of taps 5 through 7 shows that the stagnation point moves downward. The range of motion is shown in Figure 21. The total downward excursion is 18.5 mm over a body half-height of 82.6 mm. There is a suggestion that the rate of stagnation point movement begins to decrease at a ride height of (h₁ / H) \approx 0.062, which is the height at which downforce stops increasing.

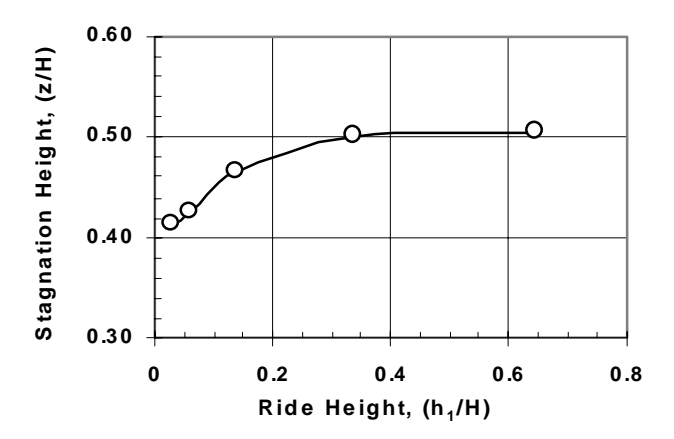


Figure 21. Variation of Stagnation Point Vertical Position with Ride Height, Fixed Ground

An immediate effect of this movement is that flow curvature in the stream tube entering the underbody region decreases. The result of this is the increase in forebody pressures observed over the lower part of the model seen in Figure 18. At the same time, the flow curvature at the upper part of the model increases and lowers the top (and presumably the side) pressure coefficients slightly. These flow displacements and curvature changes may lead to a small drag rise on the forebody.

As seen in Figure 19, the location of the stagnation point is invariant with changes in diffuser angle at constant ride height.

In summation, the measured pressure distributions provide a qualitative correlation with the observed force changes due to variations in ride height, diffuser angle and ground motion.

PRESSURE FORCES

If the pressure distributions are integrated over the major body components, it is possible to obtain a more detailed and quantitative picture of the force changes. The centre-line distribution only carries part of the pressure information on the body, but it is sufficient for a closer look at the sources of the downforce and drag characteristics that were measured.

PRESSURE-BASED DOWNFORCE – The sectional components of downforce were computed using,

$$C_L = C_L^{top} + C_L^{diffuser} + C_L^{underbody}$$
 (Eq. 12)

where,

$$C_{L}^{top} = -\frac{1}{H} \int_{0}^{L} C_{p}^{top}(x) dx$$
 (Eq. 13)

$$C_{L}^{underbody} = \frac{1}{H} \int_{0}^{L-N} C_{p}^{underbody}(x) dx$$
(Eq. 14)

$$C_{L}^{diffuser} = \frac{1}{H} \int_{(L-N)}^{L} C_{p}^{diffuser}(x) dx$$
(Eq. 15)

and L is the body length.

The term underbody refers to the body panel made up of the lower front edge and the flat part of the underbody.

Figure 22 compares the pressure-based downforce with the balance-measured downforce. The correlation is good, considering that the pressures were only measured on the model centre plane. An absolute agreement of the forces is not necessary for the purposes of this discussion. The fact that their magnitudes are so close and that they exhibit identical trends with ride height and diffuser angle justifies the use of the pressure-

based downforce components for identifying the sources of the downforce changes that were measured.

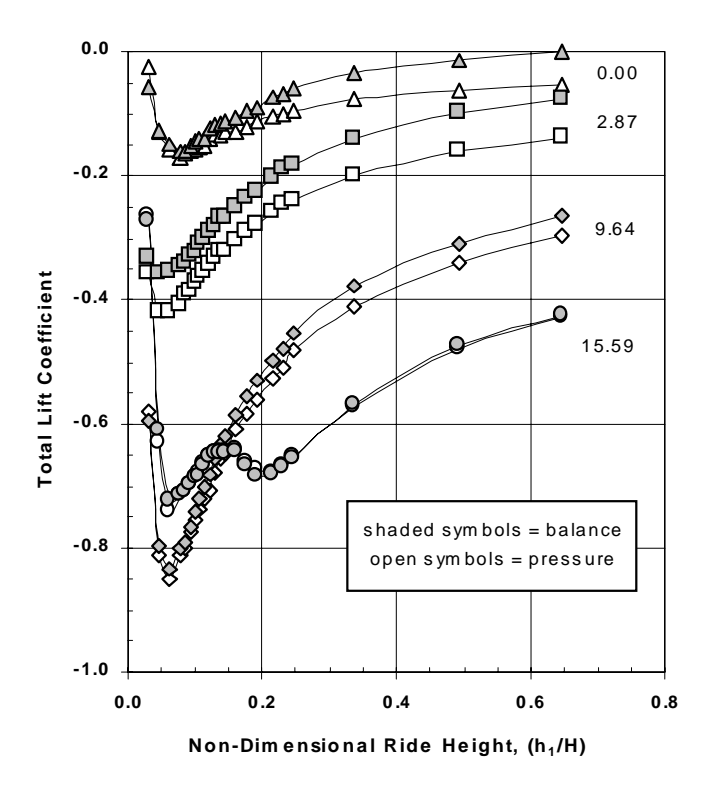


Figure 22. Comparison of Pressure-based and Balancemeasured Downforce, Ground Fixed

DOWNFORCE COMPONENTS – The pressure-based downforce components given in equations (13), (14) and (15) are presented in Figure 23.

The upper surface had positive lift, resulting from a uniform distribution of small negative pressure over the flat, upper surface and much-more-negative pressures over the upper leading edge. There is a trend for a slight reduction in upper-surface lift with increasing diffuser angle, and a larger increase in upper-surface lift with decreasing ride height at all diffuser angles. The changes are the result of changes in leading-edge pressures only. These upper-surface changes with height or diffuser angle are small compared to the underbody-induced changes.

The lower leading edge and the flat underbody contribute most of the downforce (note the difference in plot scales for all three components). The changes in downforce with ride height and diffuser angle follow the balance-force trends already discussed.

The diffuser - the last quarter of the underbody - contributes an additional, but smaller, component to the overall downforce. The effect of ride height is negligible at zero diffuser angle. The trends with ride height at the other two diffuser angles again follow the form of the flat-underbody contribution. This is not unexpected since it is the diffuser that drives a major part of the downforce-generating process.

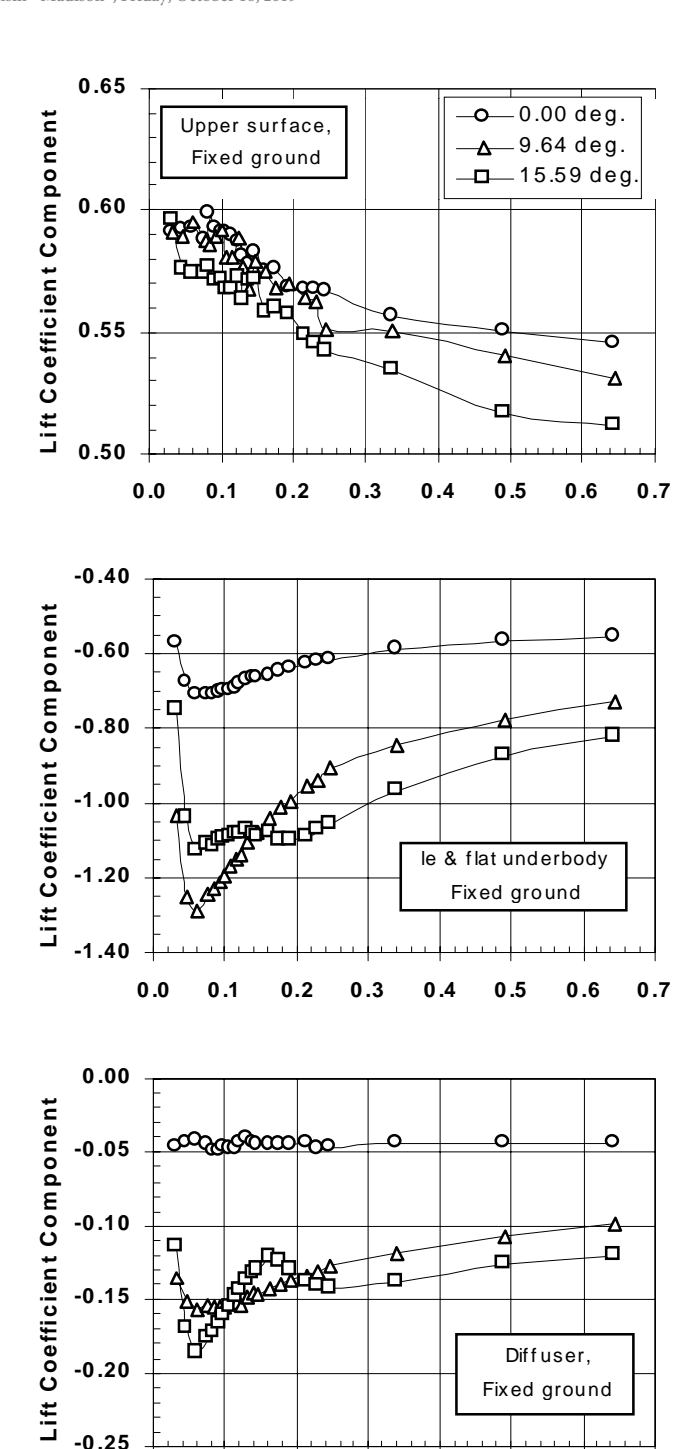


Figure 23. Pressure-based Downforce Components at Several Diffuser Angles, Ground Fixed

0.3

Non-Dimensional Ride Height, (h₁/H)

0.5

0.6

0.7

0.2

0.1

0.0

In summary, the underbody pressures dominate the downforce changes with diffuser angle and ride height. There is also a small but measurable influence from the upper front edge of the model.

The influence of ground simulation is shown in Figure 24 for a diffuser angle of 9.64 degrees. The trends shown for this angle are typical. The major effect appears in the flat-underbody force component, where ground motion

increases downforce. The diffuser downforce is also increased slightly by ground motion, although it is difficult to see at the scale used, and top-surface lift is increased somewhat.

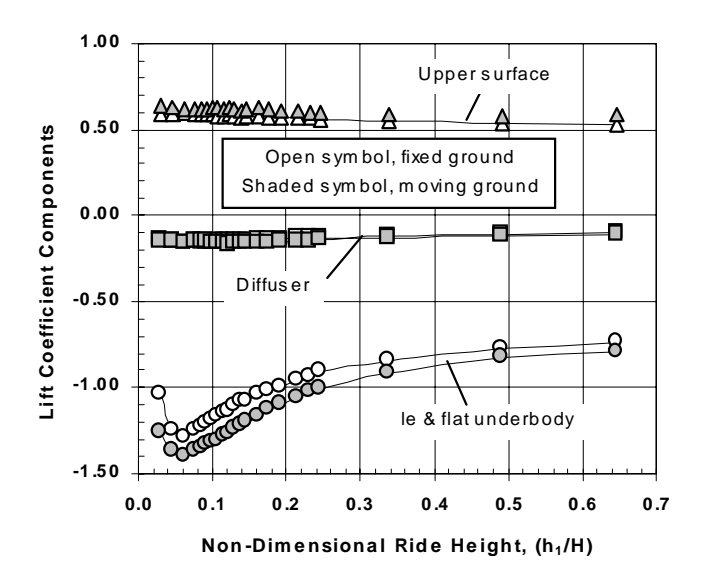


Figure 24. Effect of Ground Simulation on Pressurebased Downforce for the 9.64° Diffuser

PRESSURE-BASED DRAG – The drag forces were computed in a fashion similar to the downforces, using,

$$C_D = C_D^{front} + C_D^{diffuser} + C_D^{base}$$
 (Eq. 16)

where,

$$C_{D}^{front} = \frac{1}{H} \int_{0}^{H} C_{p}^{front}(z) dz$$

$$C_{D}^{diffuser} = -\frac{1}{H} \int_{0}^{h_{d}} C_{p}^{diffuser}(z) dz$$

$$C_{D}^{base} = -\frac{1}{H} \int_{h_{d}}^{H} C_{p}^{base}(z) dz$$
(Eq. 18)

H is the body height and h_d is the height of the vertical projection of the diffuser wall onto the plane of the model base. In this case, 'base' refers to the flat vertical panel at the rear of the model. The diffuser drag is equal to the tang component of the diffuser downforce.

Figure 25 compares the total pressure-based drag with balance measurements at the four diffuser angles of Figure 22. The agreement is not as good for drag as it was for downforce, primarily because the centre-line pressure distribution over-predicts the forebody drag, producing the shift seen.

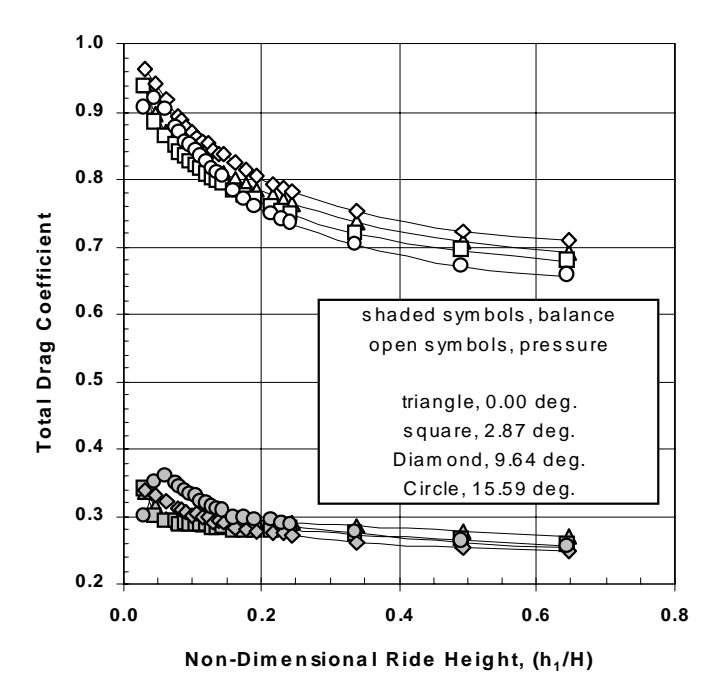
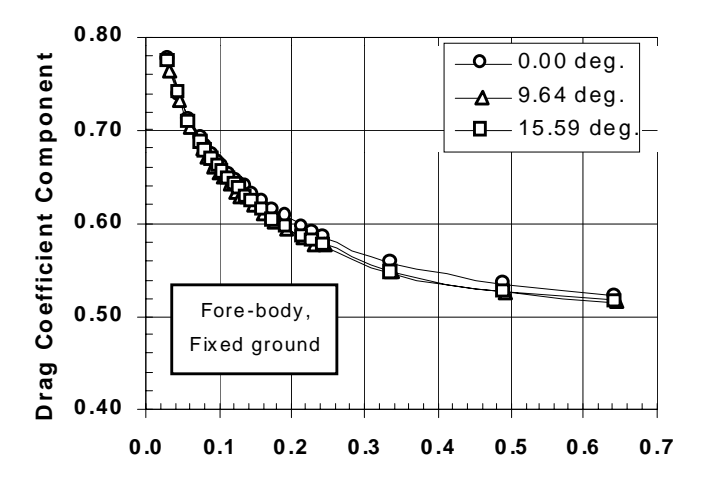


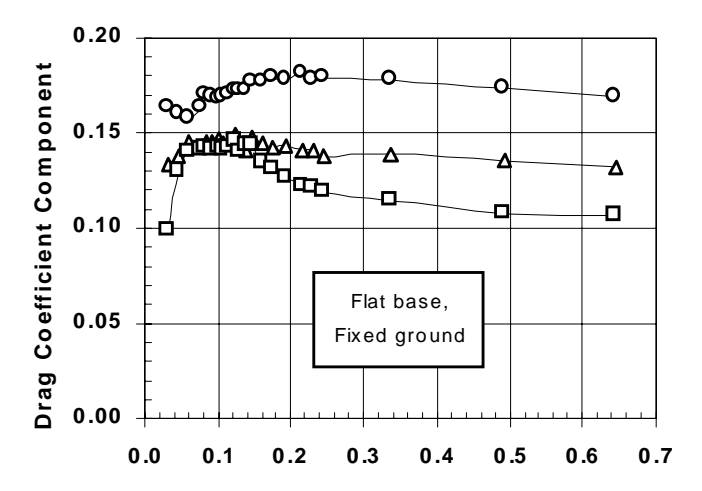
Figure 25. Comparison of Pressure-based and Balancemeasured Drag, Ground Fixed

As an example, the forebody drag coefficient at h/ H=0.646 with θ =9.64 degrees is 0.516 from the centreline integration. If it is assumed that the lateral pressure distribution behaves like the vertical pressure distribution, then the forebody drag coefficient would drop to 0.071, much closer to the value expected for a forebody with attached flow. The total pressure-based drag coefficient would decrease from 0.709 to 0.264. The main point is that the trends in the pressure-based drag coefficients are sufficiently similar to those of the force measurements that the pressure-based information can be used to help understand the observed drag behaviour.

The base-pressure measurements were obtained by pneumatically averaging the pressures over the full base area. Thus, they are an accurate measure of the base drag. It is expected that the diffuser component of drag will be approximately correct, based on the agreement in pressure-based downforce previously shown.

DRAG COMPONENTS – The three drag components of equation (16) are presented in Figure 26. The forebody drag rises monotonically with reducing ride height. Little difference is seen due to changing diffuser angle. The reason for this trend has already been given as a pressure rise over the lower half of the forebody due to the decreasing streamline curvature that occurs as the stagnation point moves downward with reducing ride height. Consequently, it represents a ground-interaction effect. Forebody drag is actually a small contributor to the total drag, as just explained in connection with Figure 25. The forebody-drag curves in Figure 26 show that the forebody drag is insensitive to diffuser angle.





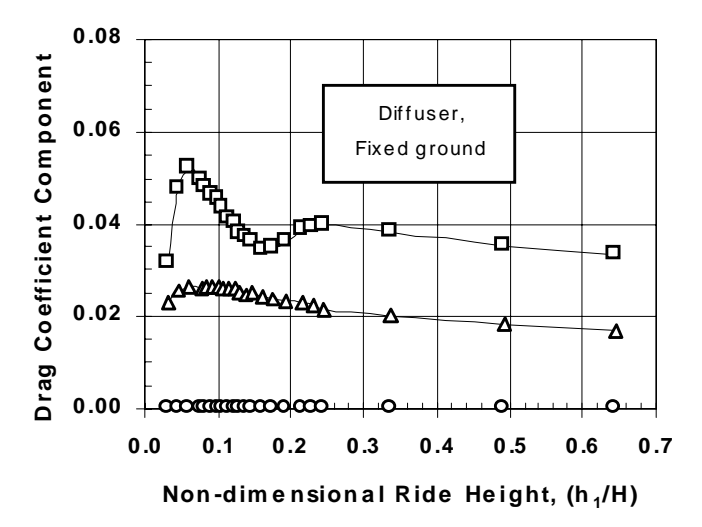


Figure 26. Pressure-based Drag Components at Several Diffuser Angles - Ground Fixed

The flat-base pressure-drag component in Figure 26 rises slightly with initial decrease in ride height from its maximum, and then decreases at the lowest ride heights. This decrease becomes larger as diffuser angle is increased. The flat-base drag component decreases monotonically with increased diffuser angle - the drag reductions being largest at the greatest ride heights.

The diffuser component of drag reflects the diffuser lift, since they are both components of the diffuser-wall pressure force. Drag initially rises with decreasing ride height before reducing at the smallest ride heights. The diffuser drag increases with diffuser angle, in part because of the lower average diffuser pressure and in part because of the larger projected diffuser area onto the base plane.

The decreases in both base drag and diffuser drag at the lowest ride heights occur at the non-dimensional height of 0.062, the same value at which the drag for the zero-angle diffuser increased rapidly.

The large difference in measured drag between the fixed and moving grounds at low ride heights and zero diffuser angle in Figure 16 is not reflected by the pressure drag. As seen in Figure 27, both the fixed-ground and the moving-ground data are nearly identical, with only a small decrease in forebody drag and a small increase in base drag caused by ground motion. The conclusion to be drawn is that the drag difference in Figure 16 must be due to a difference in viscous effects in the underbody channel that are not captured by the centreline pressures.

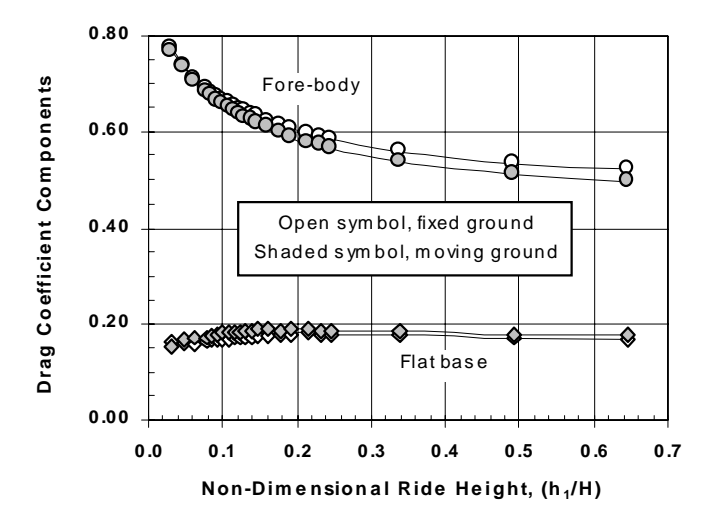


Figure 27. Effect of Ground Simulation on Pressurebased Drag for the Zero-Angle Diffuser

DIFFUSER-PERFORMANCE ANALYSIS

The data presented to this point provide an appreciation for the influence of the diffuser on the lift and drag of the model. It has been shown that the presence of an underbody diffuser affects the flowfield over the whole body, but that the major effects are in the underbody region. The preceding discussions have examined the force components on the body but have not fully extracted the diffuser behaviour from the overall effects in a fashion that will permit the diffuser flow physics to be clearly seen. The following sections will attempt to do so and, in the process, will offer a new view of the automotive diffuser from the perspective of classical diffuser physics.

This analysis will proceed by separating the measurements into diffuser and non-diffuser components. The

diffuser-based force components that remain will then be correlated with the area-ratio parameter, (AR-1), and non-dimensional length, (N/h_1) , allowing them to be interpreted in the light of the current understanding of diffuser physics.

The physical significance of these governing non-dimensional parameters is the following. The area ratio establishes the upper limit of diffuser pressure recovery, while the non-dimensional length determines the rate of pressure recovery, thus establishing the magnitude of the adverse pressure gradient in the diffuser. The shorter the non-dimensional length, the greater the pressure gradient for any area ratio. If the adverse pressure gradient is greater than that which the boundary layers on the diffuser walls can tolerate, then those boundary layers will separate from the walls, stall the diffuser, and abruptly reduce its pressure recovery.

DOWNFORCE BEHAVIOUR – A lift force is generated on a body only when the flow over the body is not symmetrical about a plane perpendicular to the lift direction. Flow asymmetry can result from the body having an asymmetrical shape or from being inclined to the flow. In the aeronautical sense, it is described by the concept of circulation.

A surface vehicle can produce lift due to shape asymmetry or body attitude, as does a wing. It can also develop lift in ground effect due to the constraining effect of the ground boundary producing an asymmetrical flow over the vehicle. This lift will occur even for a symmetrical body, and can be further modified by changes in body shape.

One example of such shaping is the introduction of an upsweep on the rear underbody that produces downforces far away from ground. The flowfield is identical to that over a slant-back body, as studied by Morel [17], except that the vertical force is downward. At large ground clearance, where the area ratio is very close to unity, the upsweep will not act as a diffuser. As this body is brought closer to the ground, however, the area ratio increases from close to unity, and the flow beneath the vehicle undergoes a gradual transition from an external flow over the bottom surface to an internal flow through an underbody channel terminated by a diffuser.

It would appear that three lift mechanisms are present on a road vehicle close to ground, excluding non-zero pitch angles. One occurs even for a symmetrical shape and will be termed 'ground interaction'. The second results from shape asymmetry, in this case due to rear underbody upsweep, and will be termed 'underbody upsweep'. The third results from additional lift components induced by the upswept underbody behaving as a diffuser, and will be termed 'diffuser pumping' since the main effect of the diffuser is to draw more flow through the underbody flow path.

Thus, the total lift can be written as,

$$C_{L} = C_{Lg} + C_{Lu} + C_{Ld}$$
 (Eq. 20)

where C_{Lg} , C_{Lu} and C_{Ld} are the contributions from ground interaction, underbody upsweep and diffuser pumping, respectively.

Ground Interaction – The downforce component due to ground interaction was assumed to be the downforce measured with the flat underbody and can be seen as the upper curve in Figure 28. It is zero at large ride height, increases with reducing ride height to a maximum, before reducing at the lowest ride heights due to viscous effects.

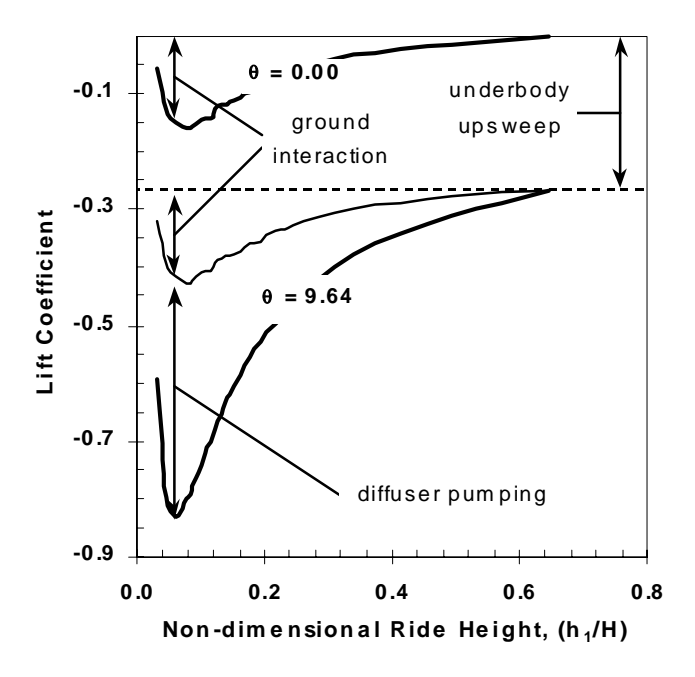


Figure 28. Identification of the Downforce Components

<u>Underbody upsweep</u> – The effect of upsweep far from the ground is to produce downforce on the model, due to the upsweep producing a cambered shape. This effect can be seen in the monotonic increase in downforce with upsweep (diffuser) angle at the greatest ride height, out of ground effect, in Figures 11 and 12. This variation is plotted in Figure 29, where it is seen to be linear and virtually identical for both ground simulations. The slope of the curve is almost identical in magnitude to that found by Morel [17] for a simple, fast-back car model generically similar to that of the present study. The downforce component due to upsweep is identified in Figure 28, using the 9.64 degree diffuser angle as typical.

<u>Diffuser pumping</u> – A powerful mechanism in the generation of downforce is the increase in flow rate under the model due to the influence of the diffuser. The literature of subsonic diffusers [7,8] indicates that diffuser angle is not a primary diffuser parameter. The principal parameters are the area ratio parameter, (AR-1), and non-dimensional length, (N/h_1) .

<u>Diffuser-downforce Separation</u> – The downforce-separation process defined in Figure 28 and by equation (20) was applied to the lift data of Figures 11 and 12. The results are the diffuser lift curves presented in Figures 30 and 31.

Each of these Figures presents a well-ordered family of parametric curves, with non-dimensional length as parameter, that have a common generic shape. Each curve has an optimum area ratio at which maximum downforce is produced. Furthermore, in the regions of area ratio smaller than the local optimum, the individual curves almost collapse to a common curve. The diffuser-based downforce is approximately one-half the total measured.

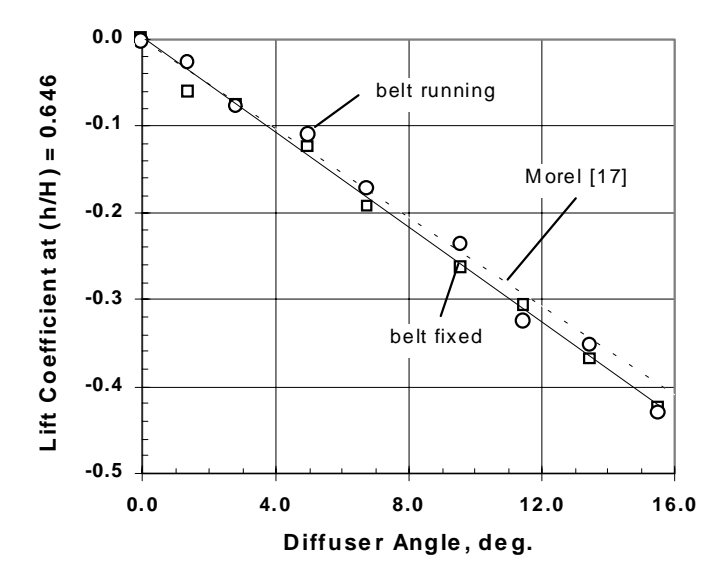


Figure 29. Effect of Underbody Upsweep on Downforce Out of Ground Effect

The data of Figures 30 and 31 can also be presented in the form of the diffuser map of Figure 4. It will be assumed that C_{Ld} is a viable surrogate for the pressure-recovery coefficient \overline{C}_p , to which it must be directly related. This is desirable because there is uncertainty in generating values of \overline{C}_p from the current data since appropriate values of p_1 and \overline{U}_1 for equation (1) are difficult to define. Figures 32 and 33 show the result for the fixed-ground and moving-ground simulations, respectively.

In contrast to Figure 4, the parametric contours are closed rather than open. This is a consequence of the maximum non-dimensional length being twice as large as for the data of Figure 4. As will be seen later, diffusers can be too long as well as too short for their area ratio.

It is clear from Figures 32 and 33 that, as the area-ratio parameter increases from zero, the diffuser-based downforce increases to a maximum and then decreases. This occurs for all non-dimensional lengths in the test range, and is the behaviour observed in Figures 30 and 31. Also, since the lower surfaces of the diffuser-based-downforce contours are relatively flat and horizontal, the

variation of diffuser-based downforce with area-ratio parameter to its maximum is essentially independent of ride height. This causes the collapse of the curves in the pre-maximum region observed in Figures 31 and 32. Finally, the value of maximum diffuser-based downforce at fixed ride height increases as non-dimensional diffuser length increases from its minimum value, reaches a maximum at $(N / h_1) = 9.42$ for the fixed-ground case, and then decreases with further increases in ride height. Again, this is the type of variation observed in Figures 30 and 31.

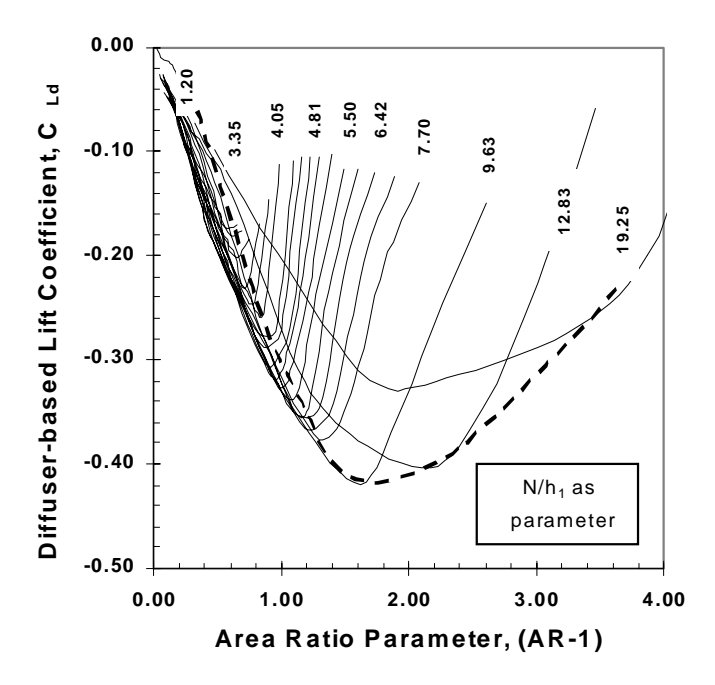


Figure 30. Parametric Plot of Diffuser-based Downforce for the Short Diffuser, Fixed Ground

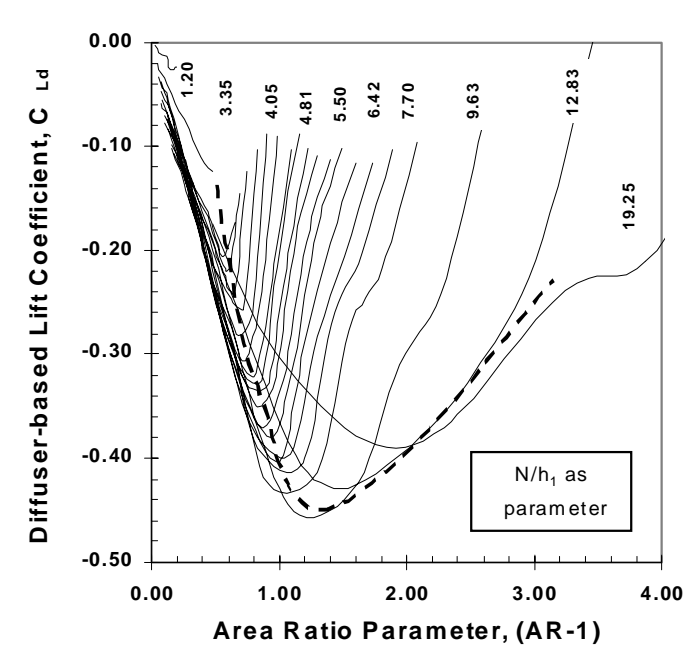


Figure 31. Parametric Plot of Diffuser-based Downforce for the Short Diffuser, Belt Running

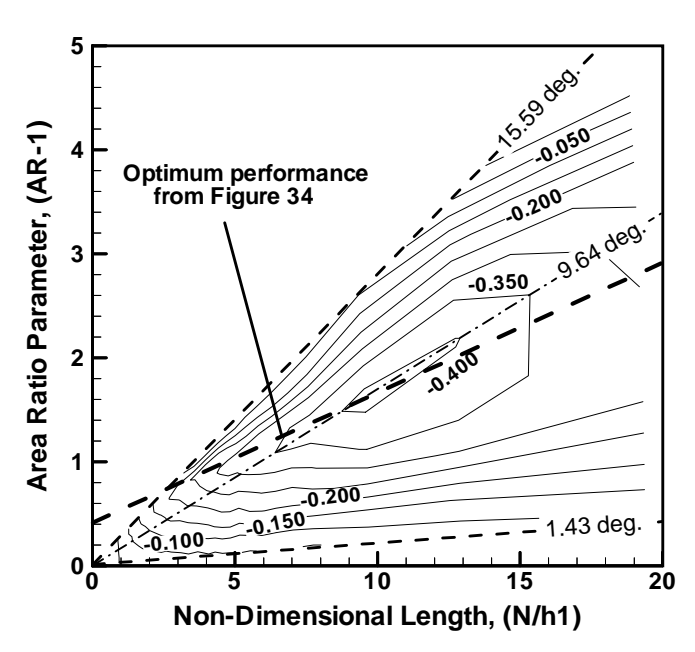


Figure 32. Contours of Diffuser-Based Downforce, Fixed-Ground

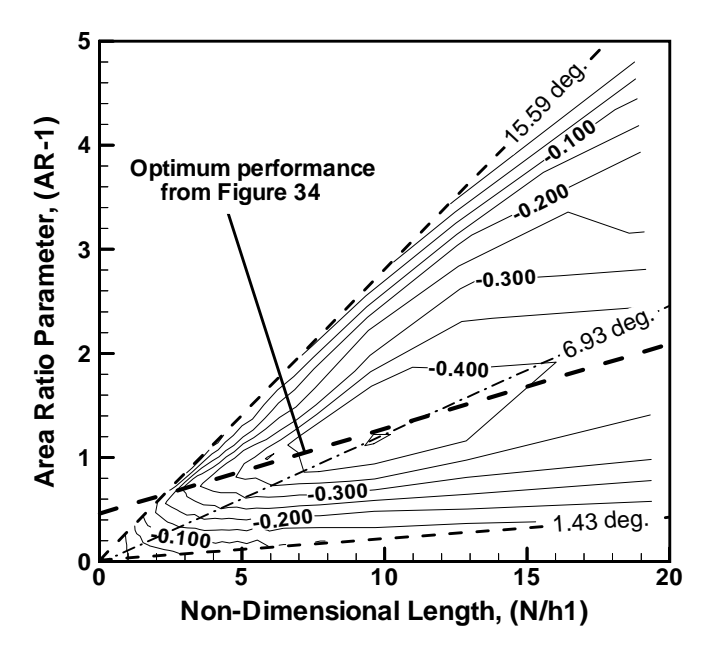


Figure 33. Contours of Diffuser-Based Downforce, Moving-Ground

In order to understand the physics behind the closed contours of diffuser-based downforce, it is necessary to examine the fundamental mechanisms of diffuser operation. The concept of flow-area blockage in internal flow systems due to a non-uniform velocity profile across the flow stream has already been introduced in the section on diffuser fundamentals. For any cross-section, the blocked-area fraction is given by,

$$B = \frac{1}{A} \int_{0}^{A} \left(1 - \frac{u}{U} \right) da$$
 (Eq. 4)

where u is the local velocity and U is the maximum velocity at the cross section. The corresponding effective cross-sectional area is,

$$A_e \equiv A(1-B) \tag{Eq. 21}$$

In diffuser applications the inlet blockage, B_1 , is greater than zero, usually because of boundary layers on the walls of the inlet channel. There are two mechanisms by which the blockage will grow within the diffuser, that is, by which the velocity profile non-uniformity will increase. The first is an inviscid one. The changes in static pressure and velocity along any streamtube of an incompressible flow are governed by Bernoulli's equation, so that,

$$du = -\left(\frac{dp}{\rho u}\right) \tag{Eq. 22}$$

Since the static pressure is essentially constant over any cross-section in the absence of flow curvature, all streamtubes must experience the same pressure change in passing between the same two stations along the flow path. Equation (22) indicates that the change in velocity required along each streamtube is inversely proportional to the local velocity level. In diffusing flows, where the pressure change, dp, is positive, velocity reductions occur and, since the magnitude of the reduction is greatest where the local velocity is smallest, the velocity differences across the stream are accentuated and the profile made more distorted, increasing the blockage.

Viscous effects also cause blockage to increase within a diffuser. Wall boundary layers grow with increasing flow distance, especially in a positive pressure gradient. As a result, their velocity profiles occupy a greater and greater fraction at any flow cross-section.

In internal flows the maximum velocity U in a cross-section is related to the blockage. Considering the volume flow rate,

$$Q = \int_{0}^{A} u da = \int_{0}^{A} \left[U - (U - u) \right] da = UA - U \int_{0}^{A} (1 - \frac{u}{U}) da$$

$$Q = UA \left[1 - \frac{1}{A} \int_{A}^{A} \left(1 - \frac{u}{U} \right) da \right] = UA(1 - B)$$
(Eq. 23)

This equation shows, for any given flow rate, that the larger the blockage the larger will be the magnitude of the maximum velocity at any cross-section. It is the reduction in maximum velocity in diffusers that is responsible for the rise in static pressure. Continuity requires that Q

be constant through the diffuser. Therefore, applying equation (23) at the diffuser inlet and outlet stations '1' and '2', respectively, gives,

$$\frac{U_1}{U_2} = \frac{A_2(1 - B_2)}{A_1(1 - B_1)} = AR \left[\frac{1 - B_2}{1 - B_1} \right] = AR_e$$
 (Eq. 24)

where AR_e is the effective area ratio. Since, as hasbeen discussed, B_2 is always greater than B_1 , it follows that AR_e is always less than the geometric area ratio, AR.

Viscous losses have not been addressed in this analysis. They can also affect pressure recovery but are usually secondary compared to the influence of velocity-profile blockage. The major reason that diffusers fail to achieve their inviscid, one-dimensional, pressure-rise potential is insufficient diffusion due to the effective area ratio being smaller than the geometric area ratio, rather than to inefficient diffusion.

With the preceding in hand, the closed nature of the diffuser-based downforce contours in Figures 32 and 33 can now be addressed. The physics can be seen most clearly by considering a q=constant line in those Figures, for example, θ =9.64 degrees in the fixed-ground case. Starting from the minimum value of diffuser non-dimensional length, the area ratio increases as the diffuser is

lengthened. For the reasons discussed above, (B_2/B_1) is greater than unity and also increases. Initially, the increase in area ratio exceeds the increase in blockage, and so the effective area ratio increases until the pressure rise and diffuser-based downforce are each a maximum. With further increases in diffuser non-dimensional length, the growth of blockage exceeds that of the area ratio so that the effective area ratio decreases, reducing pressure recovery and the resultant downforce, thereby closing the C_{Ld} contour.

<u>Loci of Optimum Diffuser-based Downforce</u> – Loci of optimum diffuser geometry have been identified by Sovran & Klomp [7]. The locus most relevant to the present study is the C_p line. It represents diffuser geometries giving maximum pressure-recovery coefficient at fixed non-dimensional length. In applications where pressure recovery is the major objective, and the diffuser length is prescribed, it defines the optimum area ratio.

In the present study, the comparable locus is the enveloping curve that follows the point of maximum downforce on each of the fixed-non-dimensional-length curves of Figures 30 and 31. As such, it closely parallels the lower boundary of those families of curves. This optimum diffuser-based-downforce locus is termed the C_{Ld}^{\star} line and is shown as a bold dashed line in each of these Figures.

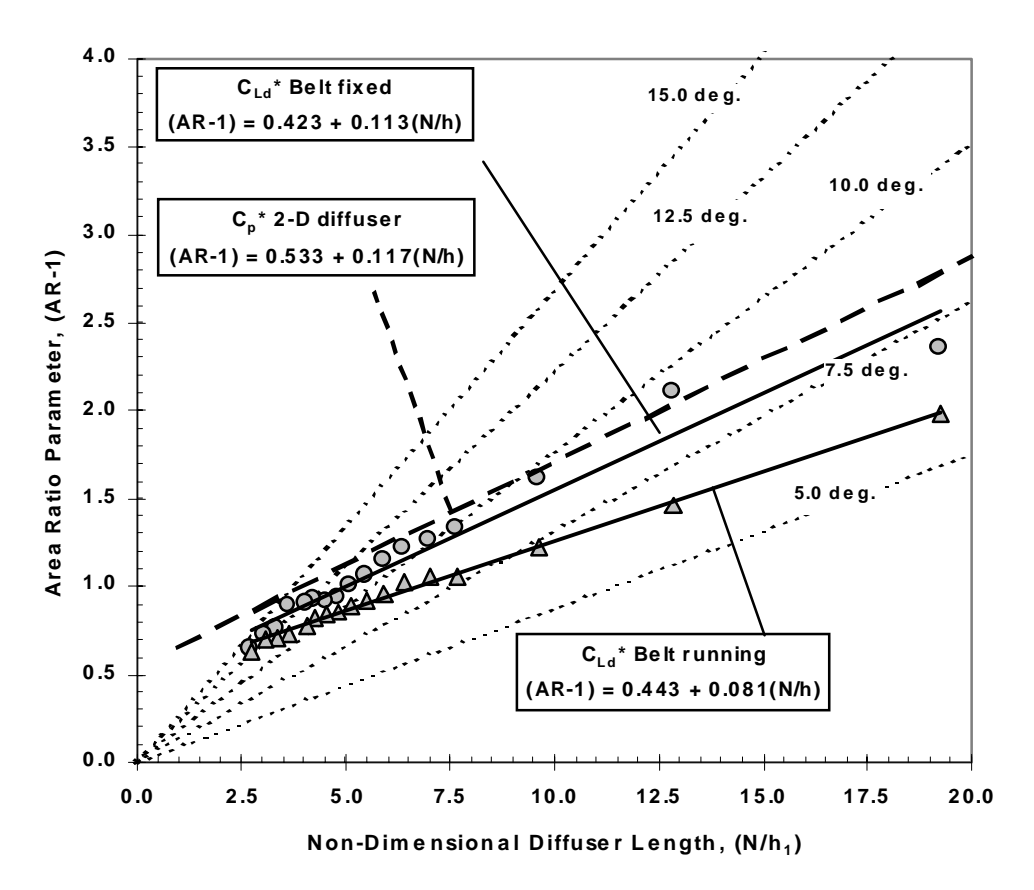


Figure 34. Loci of Geometries for Optimum Diffuser-based Downforce

These loci are transferred to the [(AR-1), (N / h_1)] plane in Figure 34. These are the fundamental diffuser coordinates used for the contour plots of Figures 32 and 33. In this case, the contour lines have been excluded for clarity. If they had been included, it would be seen that the optimum \mathbf{C}_{Ld}^{\star} lines run through the maximum values of diffuser-based downforce at every value of non-dimensional length. Lines of constant diffuser angle are included on Figure 34, showing that angle decreases with increasing non-dimensional diffuser length for both loci.

Both optimum loci have positive slopes, with that for the moving ground having the smaller magnitude. The two loci tend to converge at small (N / h₁), as would be expected at large ride height, since ground simulation is unimportant there. The lower position of the movingground locus indicates that, at any value of (N / h₁), maximum downforce is generated with a smaller area ratio than with the ground fixed. This difference can be explained on the basis of flow blockage in the diffuser flow path.Boundary layers are affected by the magnitude of the difference between fluid speed, U, and the speed of the adjacent solid boundary. At the diffuser inlet this speed difference is much smaller with moving ground than with fixed ground. Furthermore, as U decreases along the diffuser the speed difference decreases for both ground simulations, but is always smaller for the moving ground. For that simulation, the speed difference can even become negative, so that the boundary pulls the fluid rather than retards it. The overall impact of ground motion on boundary layer growth within the diffuser is a smaller value of (B2 / B1). Consequently, the ratio $(1 - B_2)/(1 - B_1)$ is larger with the moving boundary, resulting in a larger effective area ratio at a given geometric area ratio. Thus, the effective area ratio characterising the locus can be achieved with a smaller geometric area ratio when the ground is moving

For reference, the C_p^{\star} line for fixed-wall diffusers from [7] is also shown in Figure 34. It is almost identical to the C_{Ld}^{\star} line with the ground fixed. This is confirmation that the diffuser-based-downforce map of Figure 32 captures the basic pressure-recovery performance of the diffuser, and that the asymmetry of its geometry is not a key factor

The variations of the maximum diffuser-based downforce found along the optimum performance loci are shown in Figure 35. Here, diffuser-based downforce is plotted against the area-ratio parameter.

The downforce curves of the two loci are similar in shape, with an offset in area ratio that results from the flow blockages just discussed. The moving-ground simulation provides slightly more maximum downforce, but the difference is small. However, the two maxima occur at significantly different values of the area-ratio parameter.

These curves permit an assessment of the error in diffuser performance that would result from a fixed-ground simulation. At the area-ratio parameter of 1.6 (AR=2.6) at which the maximum downforce occurs for the fixed-ground case, the moving ground simulation is not at its optimum. At this area ratio the fixed-ground estimate over-predicts the downforce coefficient by 0.04, or about 10 percent.

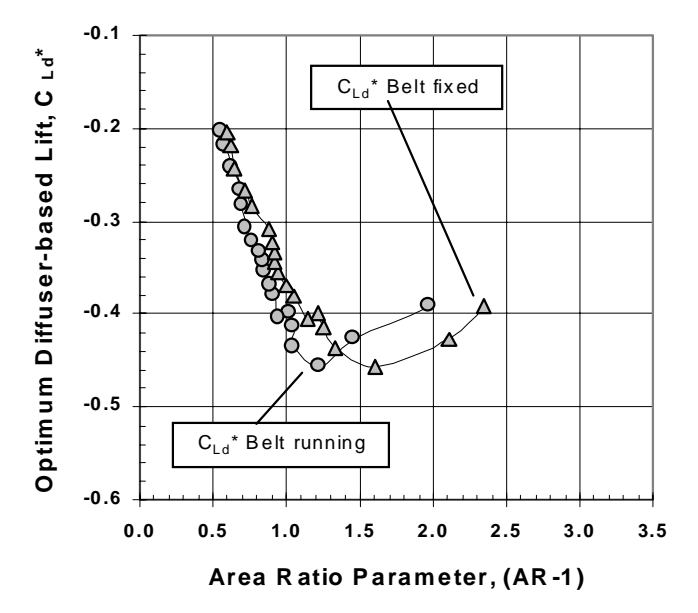
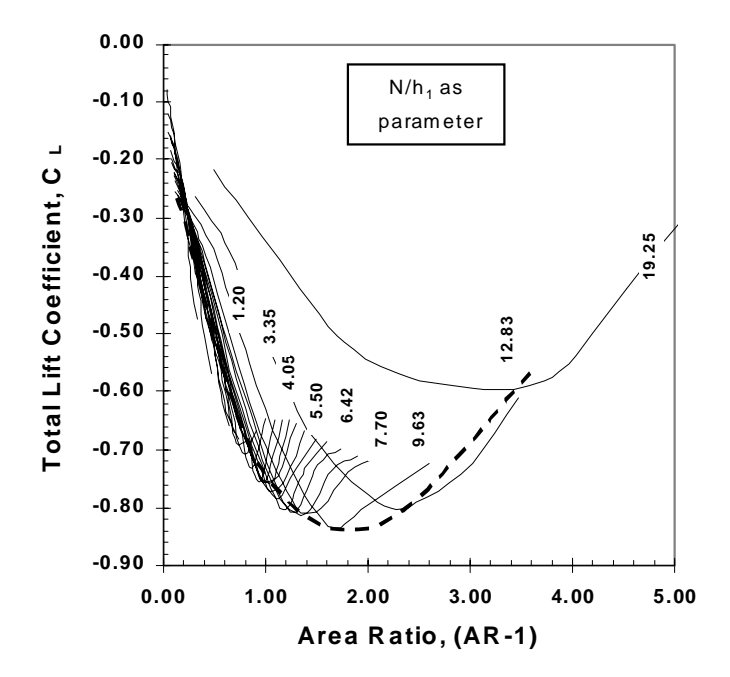


Figure 35. Maximum Diffuser-based Downforce Along the Optimum Performance Loci

Loci of Optimum Total Downforce – There are two basic questions that are relevant to whether a moving-ground simulation is required for the wind-tunnel testing of road vehicles. Firstly, does a moving ground change the underbody configuration that would be selected to achieve a desired aerodynamic performance (maximum downforce, minimum drag etc.)? Secondly, does the moving ground change the magnitude of the measured forces, and by how much and in which direction? Of these two, the first question is the more important.

Figure 34 answered the first question for the diffuser-based downforce. It showed that the diffuser designs obtained from the two ground simulations were markedly different. However, the optimum configuration should not be selected on the basis of the diffuser performance alone, since the other major downforce components due to underbody upsweep and ground interaction are missing.

When the total downforce is analysed, the loci of optimum performance are different from the loci for optimum diffuser-based downforce. These loci are presented in Figures 36 and 37 as the bold dashed lines that follow the points of maximum downforce on each successive non-dimensional-length curve. The loci are compared in Figure 38.



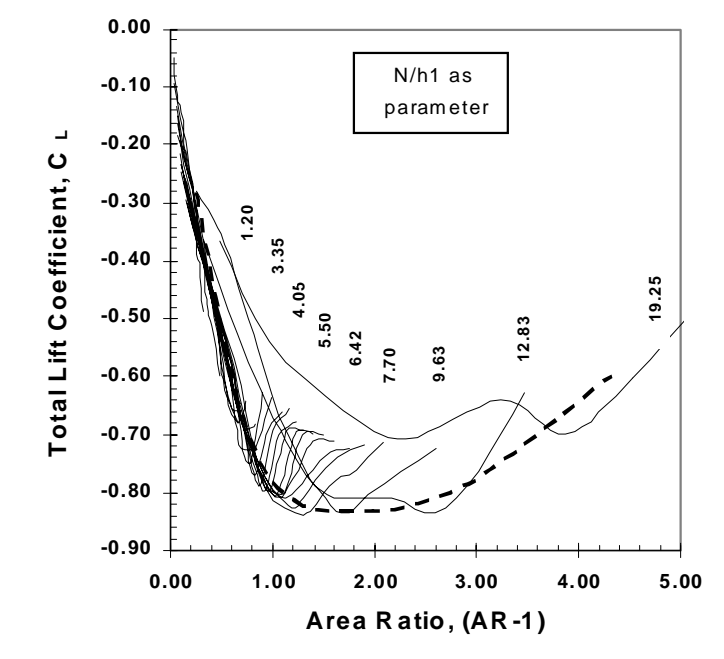


Figure 36. Parametric Plots of Total Downforce for the Short Diffuser, Fixed Ground

Figure 37. Parametric Plots of Total Downforce for the Short Diffuser, Moving Ground

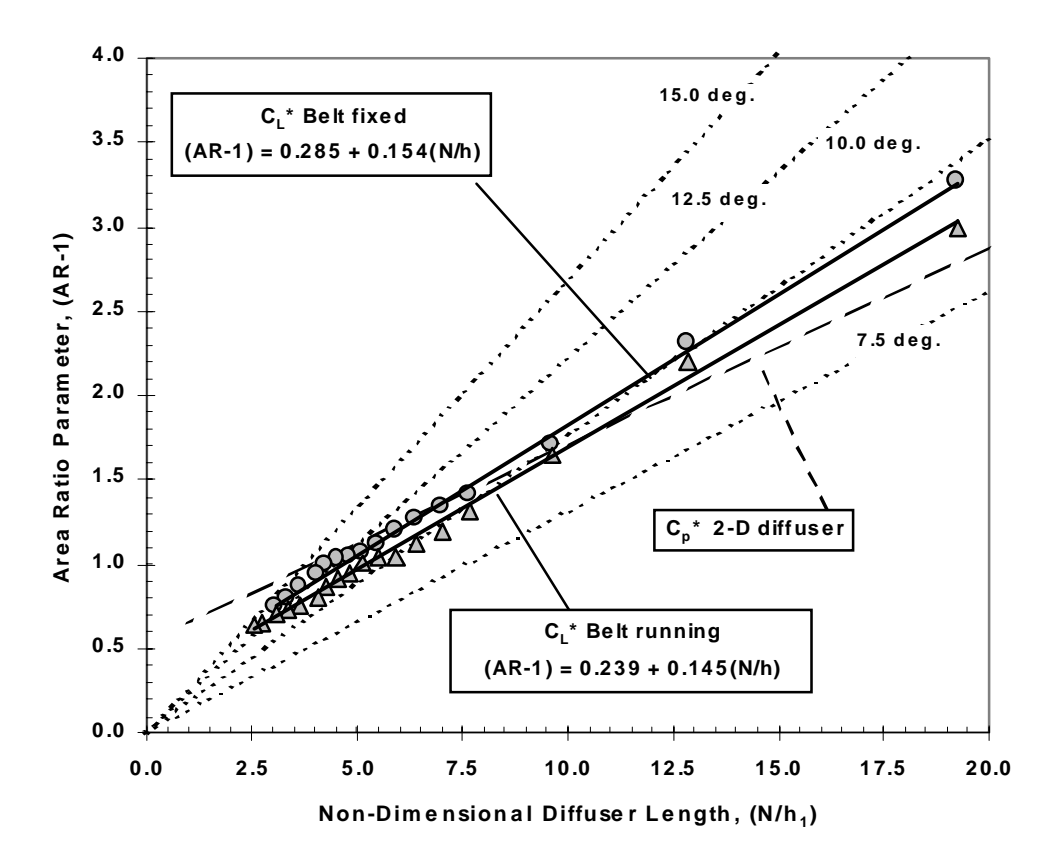


Figure 38. Loci of Geometries for Optimum Total-Downforce Performance

In Figure 38, the loci for the fixed-ground and movingground simulations are closer together than the corresponding loci for diffuser-based downforce in Figure 34. They have also moved to higher area ratios and have greater slopes than in that Figure. The reason for the movement to higher area ratios is that in the region immediately above the loci in Figure 34, the downforce increase with diffuser angle at a constant (N / h_1) is greater than the decrease of diffuser-based downforce in that Figure. Consequently, the total lift is still increasing immediately above those loci, and reaches its maximum at some point above them.

The variations of maximum total downforce along the optimum performance loci are shown in Figure 39. Compared to the diffuser-based downforce, the total downforce curves are close together and shifted to higher area ratio, as already stated. In this case, any error in diffuser design due to the use of fixed-ground simulation is small. However, the corresponding downforce is greater with the moving ground.

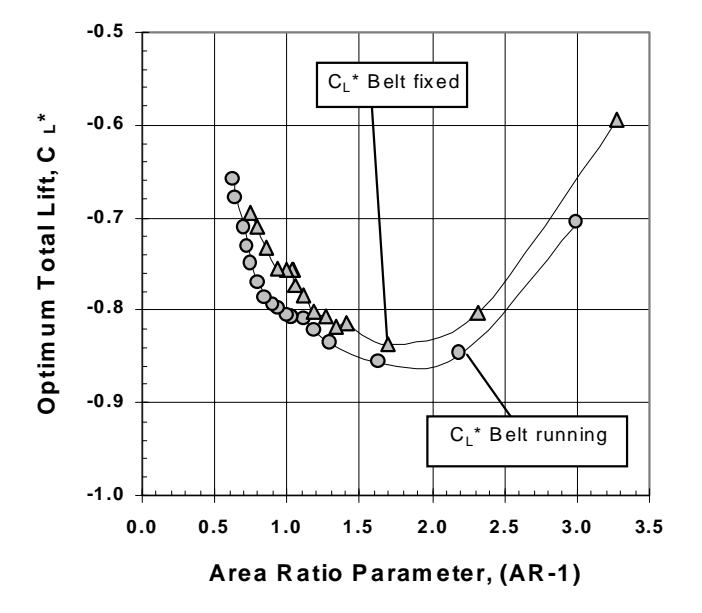


Figure 39. Maximum Total Downforce Along the Optimum Performance Loci

DRAG BEHAVIOUR

For passenger cars, the primary objective of underbody design is to reduce drag not to generate downforce. The three generic mechanisms that have been identified will be assessed with respect to their impact on drag.

UNDERBODY UPSWEEP – As has already been discussed, at large ride height, an underbody upsweep is analogous to the fastback geometry used on cars for drag reduction. Such drag reduction was documented by Janssen & Hucho [18], and its underlying physics extensively investigated by Morel [17] and Ahmed [19] using a simple body generically the same as the one used in this study. The variation of drag coefficient ratio with fastback angle from both is shown in Figure 40, with the drag minimum occurring at an angle of approximately 10 degrees.

The corresponding data from the present study (as extracted from Figures 11 and 12) is also shown in the Figure. It is seen to be consistent with the other results.

The pressure-based drag components of Figure 26 replicate the measured drag at the largest ride height and so can be used to explain the above behaviour. The influence of upsweep angle only affects the flat-base and diffuser drag components.

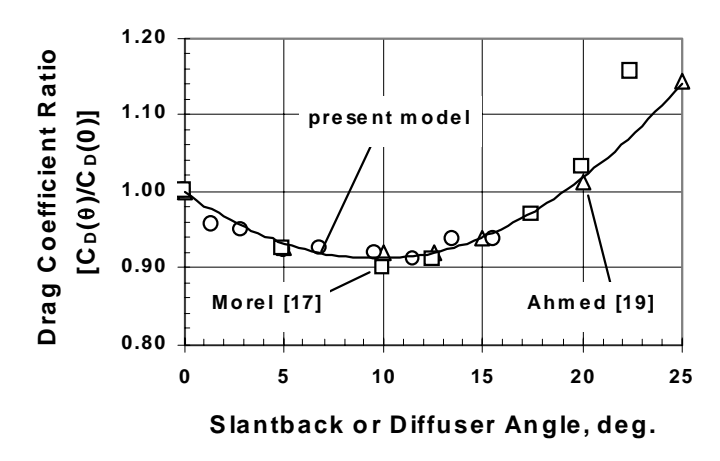


Figure 40. Effect of Fastback and Upsweep Angles on Drag at Large Ride Height

Considering the flat-base component first, the ratio of flat-base area to total base area is $1 - (N \tan \theta)/H$. For θ =9.64 degrees, for example, the flat base represents 90 percent of the area. The pressure-coefficient distributions of Figure 19 suggest no change in average flat-base pressure with upsweep angle. However, close examination of the data indicates a small pressure increase with increasing angle. When weighted by the large area fraction of the flat base, this produces the significant reductions in flat-base drag component with increasing upsweep angle shown in Figure 26. Secondly, as was indicated in the downforce discussion, the average pressure over the upswept surface decreases significantly with increasing angle, which increases the drag of this surface. However, as shown by the diffuser-drag component in Figure 26, the impact is small because of the small fraction of base area affected (note the expanded scale of the ordinate for the diffuser drag compared to that for the flat-base component in this Figure).

The net effect of the two competing drag trends is a drag reduction with increasing upsweep angle up to about 10 degrees.

DIFFUSER PUMPING – As ground clearance is reduced, diffuser pumping begins and becomes more and more effective. Diffuser pumping always increases downforce, as was seen in the preceding section on downforce behaviour.

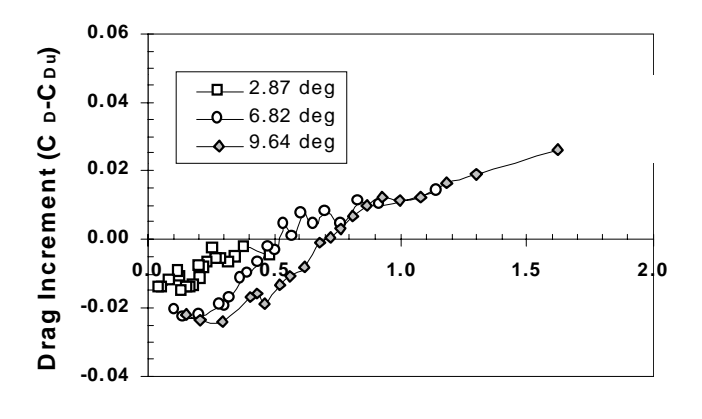
Projections of the pressures on the inclined diffuser wall produce both downforce and drag components. Consequently, the pressure-based drag and downforce components of the diffuser are related by,

$$C_D^{\text{diffuser}} = \tan \theta (-C_L^{\text{diffuser}})$$
 (Eq. 25)

Therefore, any diffuser contribution to increased down force (negative $C_L^{diffuser}$) is always accompanied by increased drag.

GROUND INTERACTION – Ground interaction has both an inviscid and a viscous influence on drag. The inviscid effect is a progressive movement of the front-face stagnation point to locations below the model centre as ground clearance is reduced (Figure 21). This increases fore-body drag. The trend is seen in the pressure-based data of Figure 26, but with exaggerated magnitude because only centre-plane pressure data are used.Underbody viscous effects become large when rideheight, (h_1 / H), is very small. Figures 13 and 14 show that the influence on drag is a small reduction from the preceding local maximum, but only to levels substantially greater than for large clearance. Another determinant of these effects is the length of the underbody flow path, (L / h_1).

The nature of the trade-off between drag-reducing upsweep and the combination of drag-increasing diffuser pumping and ground interaction is seen in Figures 41 and 42 for the two ground simulations. The data are presented only up to the area ratio of maximum drag for clarity. C_{Du} represents the drag with zero diffuser angle at each ride height.



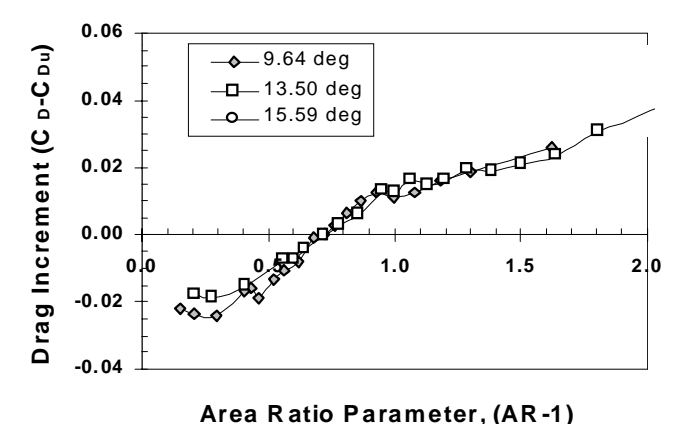


Figure 41. Drag Trade-off Between Underbody Upsweep and Diffuser Pumping, Fixed Ground

The beneficial drag reduction from underbody upsweep at large ride heights (area ratio near unity) is systematically eroded as ride height is reduced (area ratio increased), eventually becoming zero. At smaller ride heights the net effect is a drag increase. The scatter in the curves is due to experimental uncertainty.

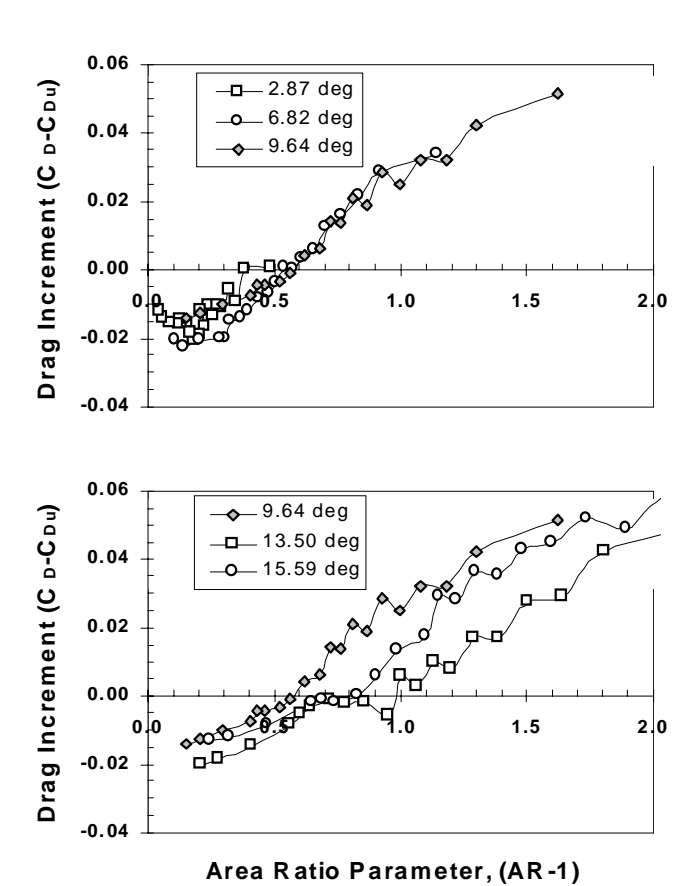


Figure 42. Drag Trade-off Between Underbody Upsweep and Diffuser Pumping, Moving Ground

In summary, from the point of view of minimising drag, ride height should not be set any lower than dictated by other considerations. However, for racing cars downforce is usually more important than drag on lower-speed courses where turns constitute a large fraction of the distance travelled. Consequently, it can be advantageous to use a small ride height for increased downforce even though it carries a drag penalty. Under such circumstances, the drag level that can be tolerated will be determined by the track and the power-to-weight ratio of the car.

TEST VARIATIONS

The main body of testing was done with endplates on the diffuser. To assess their influence, one test was made with them removed. In addition, since pitch angle is known to be an important factor in race-car set-up, several pitch variations were investigated (with endplates). The results for both variations are shown in Figure 43 for a diffuser angle of 9.17 degrees.

At large ride heights the endplates had very little effect on downforce. Only for $(h_1 / H) < 0.10$ did their elimination produce a greater downforce. Presumably, this is the result of the low-pressure cores of the trailing vortices generated at large area ratio being stronger and closer to the diffuser wall. It is possible that the difference due to endplates would increase at larger diffuser angles.

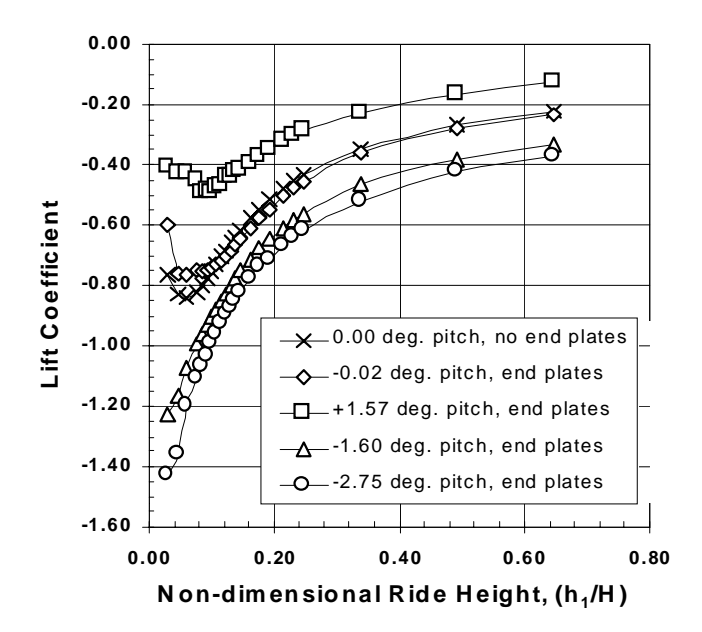


Figure 43. Effect of End-Plate Removal and Body Pitch Angle at a Diffuser Angle of 9.17 Degrees

The effect of pitch angle was significant. Positive pitch is defined as nose up, with the ride height being measured at the diffuser inlet (lowest underbody point). Negative pitch is nose down, with ride height now being measured at the front corner, again the lowest point.

Approximately one-third of the maximum downforce was generated at the largest ride height. At this ride height, the pitch changes represent changes in the approach-flow angle to a cambered body having its suction surface on the bottom. A positive pitch angle produces a positive lift increment and a reduction in total downforce from it, while a negative pitch angle produces a negative lift increment that increases total downforce. The magnitudes of the downforce increments for similar positive and negative pitch angles were nearly identical at the greatest ride height, but were much different at the lowest ride height. Here, the downforce increase with negative pitch angle was much larger than the downforce decrease with positive pitch.

The variations in downforce with reduced ride height are typical of the main body of data, except that the downforce loss at very low ride heights has disappeared with the negative pitch angle. The maximum downforce appears at the lowest ride height. The whole underbody passage is now a diffuser. The area ratio has increased only slightly, yet the maximum downforce is increased 75 percent by negative pitch.

It is thought that the expanding flow path under the flat part of the body has reduced inlet blockage and/or reduced the viscous loading of the underbody flow path by providing more room for boundary layer growth, rather than it being an increased area-ratio effect. Although the data are not presented here, the long diffuser, with a much shorter flat underbody channel, showed only a

small downforce increase with the same pitch angle changes, supporting the above argument.

CFD RESULTS

Computational methods were applied, as earlier described, to assist in understanding the data. There was also an interest in correlating the numerical predictions with experiment. The primary application of the CFD, which was performed early in the analysis phase of the results, was to examine the lift behaviour at diffuser angles above 9.64 degrees to explain the loss in downforce that occurred at ride heights in the neighbourhood of (h1 / H) = 0.20 (see Figures 11 and 12). The CFD results were also intended to provide information on the underbody velocity profiles and the resulting flow blockages

The numerical model employed had no endplates because a model without endplates was available and was thought to be adequate for these preliminary calculations.

COMPARISON OF PRESSURE DISTRIBUTIONS – The underbody centre-line pressure distributions are compared for a 9.17 degree diffuser with no endplates in Figure 44. The general behaviour of the measured pressure profiles are replicated by the CFD, with the correspondence being best at the greatest ride height. The main difference at this ride height was probably due to a laminar flow separation at the entrance to the underbody that cannot be predicted by the fully-turbulent code. There is also some difference near the start of the diffuser due to a sharper break in the wall geometry of the CFD model. At the lower ride height, the CFD slightly under-predicts the negative underbody surface pressures for both ground simulations.

In general, the trends with change in ride height and ground simulation are qualitatively and quantitatively similar to the corresponding measurements.

The predicted forebody pressure distributions are close to the measurements in all cases, and the base pressures are in reasonable agreement with the measurements.

DRAG AND DOWNFORCE – The lift and drag predictions are compared to the measurements in Figures 45 and 46. For the two 9.17-degree-diffuser-angle, movingground computations that were made, the lift is in good agreement at both ride heights, but the drag agreement is poor at the larger ride height.

These Figures also compare prediction and measurement for the 13.5-degree diffuser at five ride heights. The comparison is compromised by the lack of endplates in the CFD model. The intention was to examine the peculiar lift behaviour in Figures 11 and 12 at the larger diffuser angles and small ride heights. It was hoped that the trends in the CFD results could help understand this measured behaviour.

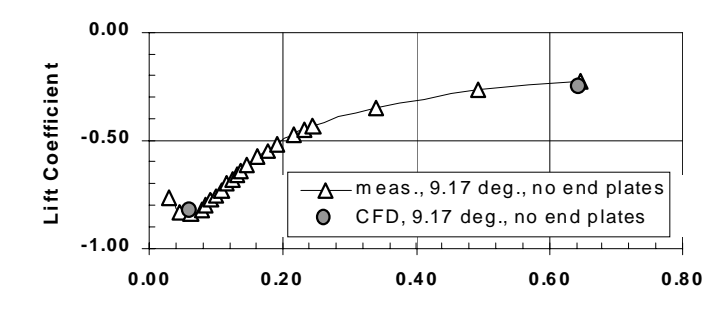
-0.10 0.00 0 10 0 20 0.30 0.40 1.0 **Pressure Coefficient** _ m eas., 0.062, fixed CFD, 0.062, fixed 0.0 -1.0 -2.0 0.00 -0.10 0.10 0.20 0.30 0.40 1.0 Pressure Coefficient _ meas., 0.062, moving CFD, 0.062, moving 0.0 -1.0 -2.0 0.00 -0.100.10 0.20 0.30 0.40 1.0 **Pressure Coefficient** 0.0 -1.0 meas., 0.646, moving CFD, 0.646, m oving -2.0

Distance from Start of Underbody, m

Figure 44. Comparison of Measured and Computed Centre-line Pressure Distributions - 9.17 Degrees, No Endplates

For the 13.5-degree diffuser, Figure 45 shows that the code agrees with the downforce measurement at the highest computed ride height of $(h_1 / H) = 0.192$. However, as ride height is reduced from this value, the computed downforce behaviour does not follow the measured trend, but continues a steady increase to the critical ride height of $(h_1 / H) = 0.062$ before decreasing. This is the type of variation measured with the smaller diffuser angles. The reason for the difference may lie in model Reynolds number. The code is fully turbulent, the model is not, as indicated by the probable separation bubble seen in the pressures of Figure 18 at the model leading edge.

On the positive side, the code accurately predicts the height at which viscous effects lead to an abrupt reduction in downforce.



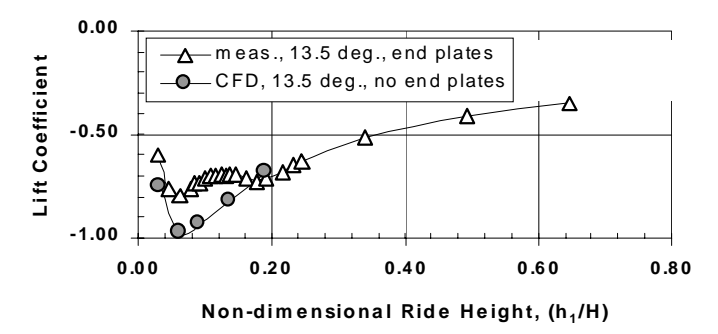
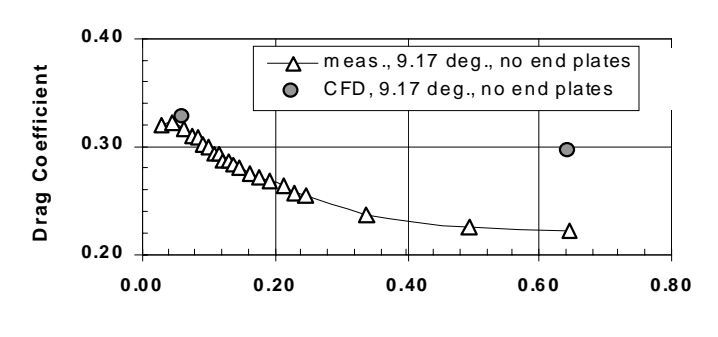


Figure 45. Comparison of Measured and Computed Downforce, Moving Ground



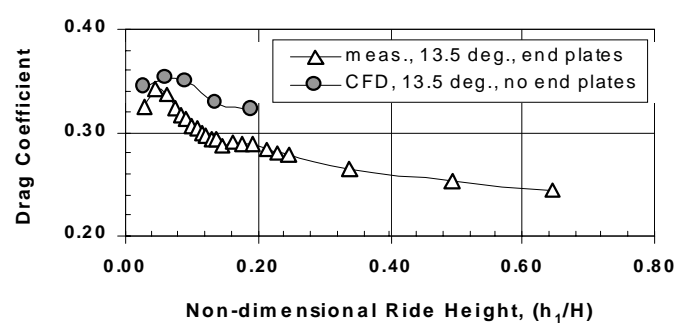


Figure 46. Comparison of Measured and Computed Drag, Moving Ground

The code prediction is very likely a better measure of high-Reynolds-number behaviour than the experiment. Interestingly, CFD would suggest that the optimum diffuser angle for maximum downforce is greater than the 9.64 degrees measured, closer to 13 degrees. Co-incidentally, modern Indy Lights cars use diffuser angles of about 13 degrees.

The drag is generally over-predicted, especially at the higher ride heights. The drag-coefficient difference at the maximum ride height appears to originate from the base

pressure. At the ride height of $(h_1/H) = 0.062$, with fixed or moving ground, the measured and predicted base pressures are nearly identical, and the drag coefficients are also close. However, when the ride height is large, the predicted base pressure is more negative than the measurement, and the drag is therefore too large. Reasons for these differences are not yet known. The base pressure comparisons are presented in Table 1, below.

Table 1. Comparison of Measured and Predicted Base-Pressure Coefficients - 9.17 Degrees

(h ₁ H)	0.062 Fixed	0.062 moving	0.646 moving
Measured	-0.160	-0.190	-0.191
CFD	-0.167	-9.182	-0.162

UNDERBODY VELOCITY PROFILES AND BLOCKAGE – In general, the CFD predictions of downforce for the 9.17-degree diffuser in Figure 45 are sufficiently good that the underbody velocity profiles should provide useful estimates of the diffuser blockage parameters - B_1 and B_2 .

The velocity profiles that were computed for the two ground simulations of the 9.17-degree diffuser are presented in Figure 47. Four profiles are shown for each case. U_0 is the free-stream velocity, z is the vertical-position coordinate measured positively upward from the ground plane and u(z) is the local velocity. The inlet profile is at the station where the flat underbody starts. The mid-underbody station is half-way between that location and the start of the diffuser. The diffuser inlet location is at the end of the diffuser.

Both graphs show similar trends. The flow velocities are highest at the inlet, diminish by the mid-underbody location, accelerate somewhat to the diffuser inlet, and decrease greatly by the diffuser exit. The velocity trend upstream of the diffuser is consistent with the pressure trend in that region seen in Figure 44. The progression of flow distortion along the flow path is evident. It is also evident that the average flow speeds with moving ground are higher than with fixed ground, especially near the ground at the end of the diffuser.

Using the centreline profiles of Figure 47, the blockage parameter defined in equation (4) was calculated at the diffuser inlet and exit locations for the two ground simulations. These blockages were then used to evaluate the effective area ratios using equation (24). The results are presented in Table 2.

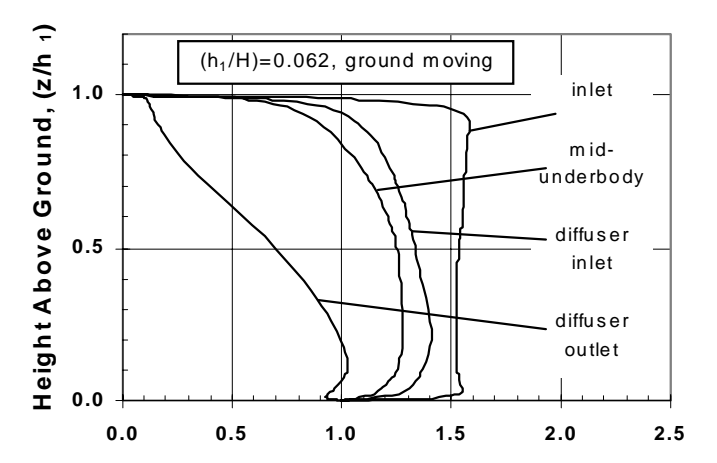
For both ground simulations, the effective area ratio is less than the geometric one. What is initially surprising is that it is smaller for the moving ground. This is traceable to its larger B2. An examination of the exit-velocity profiles shows a large difference between the two simulations in the lower half of the stream. It is a consequence of the ground speed $\rm U_0$ being greater than the fluid velocities in the end portion of the diffuser. As a result, the ground pumps energy into the stream and pulls the fluid

along. While this is beneficial in one sense, it is detrimental to the intended purpose of the diffuser, which is to slow the stream.

Table 2. Computed Diffuser Flow Blockages and Effective Area Ratios - 9.17 Degrees, No Endplates, AR=2.54

Configuration	B ₁	B ₂	(1-B ₂) (1-B ₁)	AR _e
0.062, fixed	0.100	0.281	0.80	2.03
0.062, moving	0.101	0.384	0.69	1.75

The experimental data that has been presented suggests that effective area ratio is greater for the moving ground. This apparent inconsistency between computation and experiment needs further investigation.



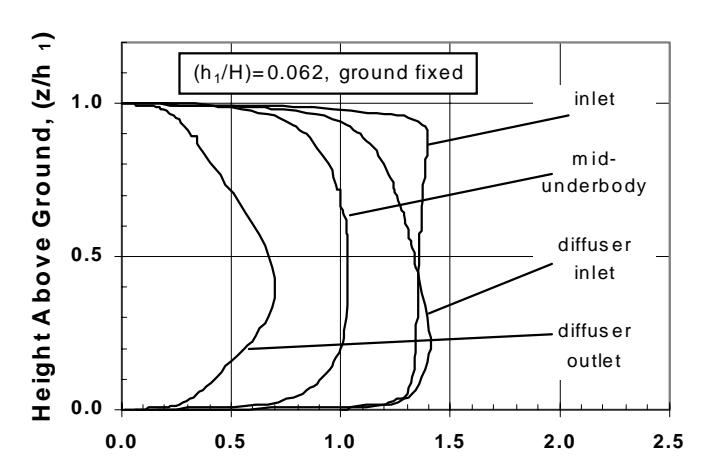


Figure 47. Underbody Centreline Velocity Profiles, 9.17
Degrees With No Endplates

UNDERBODY SURFACE FLOW – Figure 48 presents the surface flow from CFD on the front, the left side and the underbody of the model. Only one-half of the model is shown, divided at the vertical centre plane. The underbody faces downward in the image, the left side faces upward, and the front is at the right. The case shown is for the 13.5-degree diffuser at $(h_1 / H) = 0.062$ with the ground moving.

The most obvious front-face feature is the stagnation point below the model centre. The flow is seen to diverge as it enters the underbody before converging inward farther downstream. This pattern reflects the pressure distributions observed. As the diffuser is approached, the inflow strengthens and a strong vortex is formed under the rear part of the flat-bottomed section. The vortex flows under the model and grows rapidly on entry into the diffuser. The reattachment line in the diffuser is the locus from which strong flow divergence occurs. There is a small secondary vortex at the outer edge of the rear of the diffuser. The diffuser flow pattern is complex, with the surface flow curving back upstream (downward in the picture) to a separation line running across the upstream end of the diffuser wall. The outer end of this line appears to be a focus of separation from which a vortex forms and runs downstream.

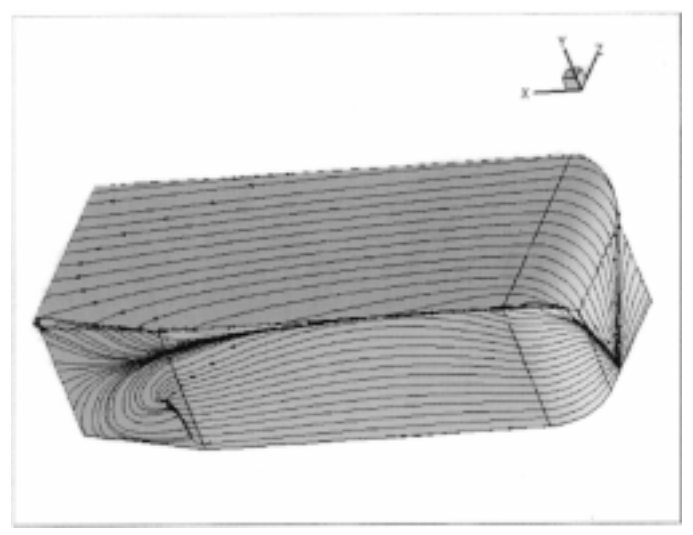


Figure 48. Computed Underbody Surface-Flow Streamlines, 13.59 Degree Diffuser, No Endplates, $(\mathbf{h}_1/\mathbf{H}) = 0.062$, Moving Ground (flow from the right)

SUMMARY

This investigation has examined the aerodynamic behaviour of plane-walled, single-plane-expansion, underbody diffusers fitted to a wind-tunnel model of a wheel-less, simple body having passenger-car proportions. An extensive data-base has been acquired, using both fixed-ground and moving-ground boundary simulations. Force-balance measurements are complemented by body-surface pressure distributions and by CFD results. The data have been analysed from a diffuser perspective by relating it to the conventional diffuser parameters of area ratio, non-dimensional length and flow-area blockage. The measured data are found to collapse on these parameters.

Three fluid-mechanical mechanisms affecting downforce and drag have been identified, and they have been quantified for the particular test model. Ground interaction is a major contributor to downforce, which is generated by the asymmetry in the model's flow-field caused by the nearby presence of a solid boundary on only one side of it.

Upsweep of the rear underbody creates a cambered body that can produce significant downforce at large ride height. It is also effective in reducing drag far from ground in the same manner as does a fast-back geometry on a passenger car.

As a body with underbody upsweep is brought close to ground, the flow underneath it undergoes a gradual transition from an external flow over a surface to an internal-flow in a channel terminated by a diffuser. The diffuser effectively acts as a pump, increasing the velocity and decreasing the pressure in the underflow, thereby augmenting the downforce on the body. However, an additional drag component is also generated by this augmented flow, and at sufficiently small ride heights it can completely negate the drag-reducing benefit of underbody upsweep, and even exceed it. Consequently, there is an inherent downforce/drag trade-off that is rideheight dependent.

Diffuser performance has been extracted from the data, and its behaviour is qualitatively similar to that in the literature of two-dimensional, plane-wall diffusers. The loci identifying the area ratios producing the greatest diffuser contribution to downforce at any given non-dimensional length has been determined for both the fixed and moving-ground boundary conditions. It is believed that these lines of optimum diffuser geometry have a significant degree of generality, and are applicable to the underbody diffusers of realistic vehicle shapes.

Since three mechanisms of downforce generation are present, optimum-geometry lines for total body downforce have also been generated. While, in principle, more applicable to vehicle design, they are body-shape dependent. Their degree of utility for realistic vehicle shapes is not known. The wheel-less nature of the test model may be a significant factor in data transferability. The wheels of actual vehicles influence the lateral flows into and out of the underbody region even when not rotating. Wheel rotation may add yet another influence to these flows.

Both types of optimum-geometry line are different for fixed-ground and moving-ground boundary simulations. The moving ground always prescribes the smaller area ratio for any given non-dimensional diffuser length.

The simplified test model of this investigation is not highly representative of the generic shapes or underbody geometries of actual passenger cars or racing cars. Nevertheless, the nature of the experiments and the type of data analysis that has been presented should be transferable to the development process for those vehicles.

The non-dimensional collapse developed for the data and the linear nature of the optimum-performance loci that were found should result in future investigations for optimum design requiring significantly fewer measurements or computations for accurate determination.

The data shows that large downforce can be generated by diffuser systems. It is also demonstrated that flat-bottomed geometries are pitch-angle sensitive, and that downforce can be nearly doubled by only a few degrees of nose-down pitch angle on the body.

Useful levels of drag reduction can be obtained by short, shallow-angle diffusers that are typical of a passenger-car installation. For this application, drag reduction would benefit from a clean, low-loss underbody flow path.

CFD was utilised to aid interpretation of the data. It suggests that some anomalous model-lift behaviour was probably due to the low test Reynolds number. The CFD results predict that maximum downforce occurs at a larger angle than indicated by the experimental results. This predicted angle is in agreement with the diffuser angles found on current Indy Lights cars, which have flat-bottomed bodies followed by diffusers.

DEDICATION – This paper is dedicated by Kevin Cooper and Gino Sovran to their friend and fellow researcher, Geoff Carr. Geoff was a vehicle aerodynamicist of the highest order, with a deep interest in the issues with which this paper deals. We would like to think that he would have approved of our work. His untimely death has ended an exciting and enjoyable, long-term collaboration. We will miss you, Geoff.

ACKNOWLEDGMENTS

The first author would like to thank his co-authors for their efforts: Genevieve Dutil who designed the model and modified the belt system; Tamas Bertenyi whose persistence and experimental abilities completed a demanding series of measurements and data analyses; Jerry Syms for squeezing in the CFD; and especially Mr. Diffuser, Gino Sovran, whose insight and quest for 'the physics' have made this a better paper than it otherwise might have been.

REFERENCES

- P.G. Wright; The Influence of Aerodynamics on the Design of Formula One Racing Cars. International Journal Of Vehicle Design, vol. 3, no.4, 1982.
- H.J. Emmelmann, H. Berneberg, J. Schulze; The Aerodynamic Development of the Opel Calibra in the DNW. SAE 900327, Detroit, February, 1990.
- E. Mercker, H.W. Knape; Ground Simulation With Moving Belt and Tangential Blowing For Full-Scale Automotive Testing in a Wind Tunnel. SAE 890367, International Congress and Exposition, Detroit, Michigan, February 29-March 4, 1998.
- E. Mercker, H.-J. Wiedemann; Comparison of Different Ground Simulation Techniques for Use in Automotive Wind Tunnels. SAE 900321, International Congress and Exposition, Detroit Michigan, February, 1990.
- A.R. George, J.E. Donis, Flow Patterns, Pressures, and Forces on the Underside of Idealized Ground Effect Vehicles.

- J.P. Howell.; The Influence of Ground Simulation on the Aerodynamics of Simple Car Shapes with an Underfloor Diffuser. Conference on Vehicle Aerodynamics, Royal Aeronautical Society. July 1994.
- G. Sovran, E.D. Klomp; Experimentally Determined Optimum Geometries for Rectilinear Diffusers With Rectangular Conical or Annular Cross-Section. Symposium on Fluid Mechanics of Internal Flow, G. Sovran editor. Elsevier Publishing, Amsterdam, 1967.
- 8. L.R. Reneau, J.P. Johnston, S.J. Kline; Performance and Design of Straight, Two-Dimensional Diffusers. Report PD-8, Thermosciences Division, Mechanical Engineering Department, Stanford University, September 1964.
- G. Sovran; The Kinematic and Fluid-Mechanic Boundary Conditions in Underbody Flow Simulation. CNR-Pininfarina Workshop on Wind Tunnel Simulation of Ground Effect, Turin, Italy, May, 1994.
- K.R. Cooper, A.A. Fediw, K.P. Garry; Development of a Moving Ground Belt System for the Study of Vehicle Aerodynamics. Conference on Vehicle Aerodynamics, Royal Aeronautical Society. July 1994.
- G.W Carr, P.D Atkin; Influence of Moving-Belt Dimensions on Vehicle Aerodynamic Forces. Symposium on Wind Tunnels and Wind Tunnel Test Techniques, The Royal Aeronautical Society. Cambridge, UK, April, 1996.
- 12. K.R. Cooper; Approaches to Ground Simulation in North America. CNR-Pininfarina Workshop on Wind Tunnel Simulation of Ground Effect, Turin, Italy, May, 1994.
- 13. Carr, private communication, 1996.
- Antonello Cogotti; Ground Effect Simulation for Full-Scale Cars in the Pininfarina Wind Tunnel. SAE 950996, International Congress and Exposition Detroit, Michigan, February, 1995.
- G.W. Carr, W. Eckert; A Further Evaluation of the Ground-Plane Suction Method for Ground Simulation in Automotive Wind Tunnels. SAE 940418, International Congress and Exposition, Detroit, Michigan, February 26-29, 1996.
- Closed-test-section Wind Tunnel Blockage for Road Vehicles. SAE SP-1176, Warrendale, PA, USA. Edited by K.R. Cooper, Jan. 1996.
- 17. T. Morel; The Effect of Base Slant on the Flow Pattern of Three-dimensional Bodies with Blunt Ends. Aerodynamic Mechanisms of Bluff Bodies and Road Vehicles, pp 191-226. Symposium held at the General Motors Research Laboratories, Detroit, USA. Edited by G. Sovran, T. Morel and W.T. Mason, Plenum Press, 1978.
- 18. L.J. Janssen, W.-H. Hucho; Aerodynamische Entwicklung von VW Golf und VW Scirocco. ATZ, Vol. 77, 1975, pp1-5.
- S.R. Ahmed, R. Ramm, G. Faltin; Some Salient Features of the Time-averaged Ground-vehicle Wake. SAE 840300, Detroit, 1984.

CONTACT

The first author can be contacted at (613) 993-1141, Fax (613) 957-4309, e-mail Kevin.Cooper@nrc.ca.